NASA TECHNICAL NOTE

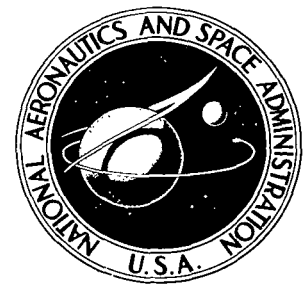

NASA TN D-6301

C. 1

TECH LIBRARY KAFB, NM
0133115

LOAN COPY: RETURN
AFWL (DOGL)
KIRTLAND AFB, N. M.

NASA TN D-6301

INVESTIGATION OF CONTROL-SURFACE INSTABILITIES ON LIFTING-BODY REENTRY VEHICLES AT A MACH NUMBER OF 15.4

by Robert C. Goetz and Frederick W. Gibson

Langley Research Center
Hampton, Va. 23365

NATIONAL AERONAUTICS AND SPACE ADMINISTRATION • WASHINGTON, D. C. • AUGUST 1971

TECH LIBRARY KAFB, NM
0133115

1. Report No.	2. Government Accession No.	3. Recipient's Catalog No.
NASA TN D-6301		

4. Title and Subtitle
INVESTIGATION OF CONTROL-SURFACE INSTABILITIES ON LIFTING-BODY REENTRY VEHICLES AT A MACH NUMBER OF 15.4

5. Report Date
August 1971

6. Performing Organization Code

7. Author(s)
Robert C. Goetz and Frederick W. Gibson

8. Performing Organization Report No.
L-7610

10. Work Unit No.
114-08-05-02

9. Performing Organization Name and Address
NASA Langley Research Center
Hampton, Va. 23365

11. Contract or Grant No.

13. Type of Report and Period Covered
Technical Note

12. Sponsoring Agency Name and Address
National Aeronautics and Space Administration
Washington, D.C. 20546

14. Sponsoring Agency Code

15. Supplementary Notes

16. Abstract

An experimental investigation was conducted primarily to determine whether a control-surface instability might exist for lifting-body reentry-vehicle configurations at a nominal Mach number of 15. Two types of tests were conducted to obtain information on flap behavior for a range of aeroelastic parameters and operating conditions. The first type involved a blunt two-dimensional model designed to explore the influence on flap response of a number of aeroelastic parameters, whereas the second type involved a more specific study of the flap behavior on a 1/30-scale model of a typical reentry vehicle.

Tests were conducted in helium flow at a Mach number of 15.4 and a Reynolds number range per meter from 23.0×10^6 to 26.2×10^6 (7×10^6 to 8×10^6 per foot) to determine the aerodynamic in-phase or stiffness coefficients and the out-of-phase or damping coefficients by the free-oscillation technique. The results indicated that, for flaps mounted on the two-dimensional model at angles of attack of 0° and 15°, the aerodynamic stiffness and damping coefficients were, in general, stabilizing. A trend of increasing amounts of damping with increasing flap angles from 0° to 70° was exhibited. The results for flaps mounted on the three-dimensional model at an angle of attack of 25° indicated an unsteady, random, nondivergent response for flap angles greater than 30° with the amplitude of the response increasing with increasing flap angles. A destabilizing trend of loss of aerodynamic damping was measured for increasing flap angles, with negative damping for flap angles greater than about 37°.

The experimental results were compared with results calculated by using both Newtonian theory and Newtonian theory including local-impact and local-wedge corrections. Although the two-dimensional results showed good agreement, the three-dimensional experimental results were not predicted.

17. Key Words (Suggested by Author(s))	18. Distribution Statement
Hypersonic control-surface instability Lifting-body reentry vehicles Unsteady aerodynamic characteristics of trailing-edge flaps	Unclassified – Unlimited

19. Security Classif. (of this report)	20. Security Classif. (of this page)	21. No. of Pages	22. Price*
Unclassified	Unclassified	54	$3.00

*For sale by the National Technical Information Service, Springfield, Virginia 22151

INVESTIGATION OF CONTROL-SURFACE INSTABILITIES ON LIFTING-BODY REENTRY VEHICLES AT A MACH NUMBER OF 15.4

By Robert C. Goetz and Frederick W. Gibson
Langley Research Center

SUMMARY

An experimental investigation was conducted primarily to determine whether a control-surface instability might exist for lifting-body reentry-vehicle configurations at a nominal Mach number of 15. Two types of tests were conducted to obtain information on flap behavior for a range of aeroelastic parameters and operating conditions. The first type involved a blunt two-dimensional model designed to explore the influence on flap response of a number of aeroelastic parameters, whereas the second type involved a more specific study of the flap behavior on a 1/30-scale model of a typical reentry vehicle.

Tests were conducted in helium flow at a Mach number of 15.4 and a Reynolds number range per meter from 23.0×10^6 to 26.2×10^6 (7×10^6 to 8×10^6 per foot) to determine the aerodynamic in-phase or stiffness coefficients and the out-of-phase or damping coefficients by the free-oscillation technique. The results indicated that, for flaps mounted on the two-dimensional model at angles of attack of 0° and 15°, the aerodynamic stiffness and damping coefficients were, in general, stabilizing. A trend of increasing amounts of damping with increasing flap angles from 0° to 70° was exhibited. The results for flaps on the three-dimensional model at an angle of attack of 25° indicated an unsteady, random, nondivergent response for flap angles greater than 30° with the amplitude of the response increasing with increasing flap angles. A destabilizing trend of loss of aerodynamic damping was measured for increasing flap angles, with negative damping for flap angles greater than about 37°.

The experimental results were compared with results calculated by using both Newtonian theory and Newtonian theory including local-impact and local-wedge corrections. Although the two-dimensional results showed good agreement, the three-dimensional experimental results were not predicted.

INTRODUCTION

Maneuverability during atmospheric reentry is important to man's projected extension of aircraft capability into outer space. Most lifting-body reentry-vehicle designs being considered to provide this maneuverability use ablation-protected aerodynamic control surfaces or flaps that provide effective trim and stability during reentry, gliding, and landing. In contrast to conventional aircraft, reentry vehicles have a more rigid structure, the control surfaces are heavier with corresponding lower frequencies, and the control surfaces are required to deflect through considerably larger angles of rotation. The rigidity of these vehicles precludes multi-degree-of-freedom flutter. However, the low control-surface frequencies and large deflection angles with associated separated flow ahead of them increase the possibility of a single-degree-of-freedom instability. Therefore, in the initial design of reentry-vehicle control surfaces, attention should be given to the rotational mode in order to avoid potential instabilities.

Oscillations of a lifting-body control flap at a Mach number M of 16, which at times appeared to be divergent, were reported in reference 1. However, since the running time of the testing facility was only about 0.004 second, the interpretation was uncertain. In a separate experimental investigation (ref. 2) conducted at Mach numbers from 15 to 23 a loss of damping in flap rotation occurred as the flap incidence was increased. Again, however, the tests were conducted in a "hot-shot tunnel" with short testing times of about 0.070 second which might have obscured the results. A more comprehensive investigation was conducted over the Mach number range from 3 to 10 and is reported in reference 3. In this investigation no occurrence of a self-sustained control-surface instability was observed. Instead, the control surfaces were observed to be driven by flow disturbances which did not involve structural coupling. The control-surface response to this excitation was a random, nondivergent oscillation. Short time segments of the randomly modulated response strongly resemble those observed in the very short time-duration tests of references 1 and 2.

Since the investigation of reference 3 was confined to the Mach number region below $M = 10$, and it is likely that the maximum dynamic pressures for representative vehicles will occur at higher speeds, further investigation seemed warranted at higher Mach numbers. Accordingly, the present study was undertaken to determine whether a control-surface instability might exist for a lifting-body configuration at a nominal Mach number of 15. The purpose was to obtain information on flap behavior over a range of operating conditions with several aeroelastic parameters. Two types of tests were conducted. The first type involved a simple two-dimensional model configuration, whereas the second type involved a more specific investigation of the flap behavior on a representative three-dimensional configuration.

Studies were conducted in helium flow at $M = 15.4$ to determine the aerodynamic in-phase or stiffness coefficients and the out-of-phase or damping coefficients for upper and lower trailing-edge control surfaces attached to a two-dimensional lifting body at angles of attack of 0^o and 15^o, and for trailing-edge flaps attached to a typical three-dimensional lifting body at angles of attack of 0^o and 25^o. Variables included a range of reduced frequencies from 0.007 to about 0.038 and a range of flap-deflection angles from 0^o to 70^o. In order to define the local flow associated with various model configurations, pressure distributions were measured on the two-dimensional model and high-speed schlieren motion pictures of the flow were obtained for all configurations. This paper presents the test results and compares them with some results calculated by using both Newtonian theory and Newtonian theory including local-impact and local-wedge corrections.

SYMBOLS

Measurements and calculations were made in the U.S. Customary Units. They are presented herein in the International System of Units (SI) with the equivalent values given parenthetically in the U.S. Customary Units.

a speed of sound

b flap average semichord

C_p pressure coefficient

d diameter of blunt nose

g_a aerodynamic damping coefficient

$g_{o,i}$ structural damping coefficient in a vacuum where $i = u,L,p,s$

$g_{t,i}$ total damping coefficient at test Mach number where $i = u,L,p,s$

$i = \sqrt{-1}$

$I_{\alpha,i}$ mass moment of inertia about the control hinge line where $i = u,L,p,s$

k reduced-frequency parameter, $\omega_{t,i}b/V$

K_α spring constant, ft-lb/rad

m_i mass of control surface where $i = u,L,p,s$

M Mach number

$\bar{N}_5$ in-phase aerodynamic stiffness coefficient

$\bar{N}_6$ out-of-phase aerodynamic damping coefficient

p local pressure

q dynamic pressure, $\rho V^2/2$

$r_{\alpha,i} = \sqrt{\frac{I_{\alpha,i}}{m_i b^2}}$ where $i = u,L,p,s$

s surface coordinate measured from model-nose stagnation point (see fig. 2)

S flap span

V velocity of the free stream

α angle of attack

β_i angle between local body surface and flap (usually referred to as flap angle) where $i = u,L,p,s$ (see figs. 2 and 3)

δ local separation-wedge angle

θ flap angular degree of freedom about axis of rotation

$\mu_i = \frac{m_i}{4\rho b^2}$ where $i = u,L,p,s$

ρ density

ϕ local angle between the free-stream flow and a line tangent to a point on the surface

$\omega_{o,i}$ natural frequency of rotation of the control surface about the hinge line in a vacuum where $i = u,L,p,s$

$\omega_{t,i}$ natural frequency of rotation of the control surface about the hinge line at test Mach number where i = u,L,p,s

Subscripts:

l local conditions

L lower flaps

p port (three-dimensional model)

s starboard (three-dimensional model)

u upper flaps

∞ free-stream conditions

A dot over a symbol indicates a derivative with respect to time.

MODELS

For the design of the models of this investigation the governing aeroelastic parameters for similitude were the inertia parameter $\mu_i r_{\alpha,i}^2$, a reduced-frequency parameter

$$k = \frac{\omega_{t,i} b}{V}$$

and the Mach number, $M = V/a$. It should be noted that thermal effects, insofar as they might have a dynamic influence on an instability, have been neglected.

Despite a diversity of practical shapes and sizes of vehicles capable of hypersonic reentry, and of means of attaining acceptable maneuverability, a flight regime of interest can be roughly defined. From such a trajectory nondimensional aeroelastic parameters of inertia and reduced frequency can be estimated. Shown in figure 1 is a typical aeroelastic corridor for a reentry flap at M = 15. The upper boundary in $\mu_i r_{\alpha,i}^2$ is representative of heavy flaps (a surface density of 146.478 kg/m^2 (30 lb/ft^2)) at high altitude (67 056 meters (220 000 feet)), whereas the lower boundary is for light flaps (a surface density of 48.826 kg/m^2 (10 lb/ft^2)) at low altitude (42 672 meters (140 000 feet)). The lower boundary in reduced frequency k is representative of small, flexible, low-frequency flaps, whereas the upper boundary in k is representative of larger, stiffer, high-frequency flaps. The flaps of the present study were designed to be in the range of

frequency and inertia parameters given in figure 1, and the actual test points achieved in comparison with the typical flight boundary are presented in the figure.

The two basic model configurations tested are shown in figures 2 and 3. Illustrated in these figures are the general geometry, details of the flaps and the methods of their support, and flap-angle and angle-of-attack references. Also shown are the locations of the 10 orifices for the surface-pressure measurements on the two-dimensional model.

The two-dimensional model is a hollow, circularly blunted wedge having an angle of $27\frac{1}{2}^{\circ}$, a length of 4.01 centimeters (1.58 inches), and a span of 11.43 centimeters (4.50 inches). The model has both upper and lower 10.8-centimeter span flaps (4.25 inches) at the rear of the wedge. This configuration was tested with flaps having both slotted and unslotted leading edges. (See fig. 2.) The flaps were machined from aluminum and mounted to the forebody with rigid mounting blocks at the rear of the model. The flap stiffness was controlled by the thickness of a groove forming the hinge, and inertia was controlled by mass ballast located near the flap trailing edge. Variations in flap inertia, stiffness, and deflection angle were achieved with exchangeable flaps. Table I lists the physical parameters of the flaps tested on the two-dimensional model. The masses and inertias were determined experimentally and include the contributions of the hinges.

The three-dimensional model represents approximately a 1/30-scale version of a representative lifting-body vehicle and includes two flexible flaps on the trailing edge. (See fig. 3.) This configuration was tested with the flap leading edge sealed along its span. The flaps had an integral aluminum insert of variable thickness to control the flap stiffness. The insert was rigidly clamped to the vehicle and was covered with balsa aft of the hinge line to form the flap airfoil contour. The mass and inertia were held constant for all the flaps tested, and variations in stiffness and deflection were achieved by exchangeable flaps. The physical and dynamic characteristics of the flaps are presented in table II.

APPARATUS AND TESTS

The tests were conducted in the 60.96-centimeter-diameter (24-inch) leg of the Langley hypersonic aeroelasticity tunnel, which uses helium as a test medium. This tunnel has a contoured nozzle designed to generate a uniform test-section flow at a Mach number of about 15 and a maximum Reynolds number per meter of 27.4×10^6 (8.35×10^6 per foot). A description of this facility and its operating characteristics can be found in reference 4. Both of the model configurations were mounted in the test section on a sting-support system located along the center line of the tunnel as indicated in figures 4(a) and 5(a). For the tests the models were protected from the starting and

stopping transients of the tunnel flow by a wedge located upstream of the model as shown in figure 4(b). This collapsible wedge was retracted to a position flat against the tunnel top wall during the data-acquisition portion of the run.

Surface pressures on the two-dimensional model were measured with miniature differential pressure transducers. These gages were all located inside the model, as shown in figure 4(c), allowing flush-to-the-surface installation to minimize the pressure lag times. They were all calibrated simultaneously with the reference pressure increments in both ascending and descending order, before and after each test run, so that nonlinearity and hysteresis effects could be determined.

Strain gages used to measure flap motion were installed on the hinges of all the flaps mounted on both model configurations. A solenoid-actuated flap-exciter mechanism was positioned just aft of the flap trailing edges and was attached to the model-support sting as shown in figures 4(a) and 5(b). This mechanism was provided so that the flaps could be remotely excited in the tunnel while allowing the flaps to be unrestrained prior to and after excitation.

The operating procedure was similar for both model configurations. After the model was installed at the desired angle of attack, with the flaps in the testing attitude, the tunnel was evacuated to a low pressure. The zero-airspeed flap frequency and damping decrements were obtained by exciting the flaps. When the flap response had completely decayed, a control valve upstream of the test section was opened and flow was established at a constant Mach number and a low dynamic pressure. At this time, the model was exposed to the flow by removing the model protector wedge and the flap response to this transient was allowed to decay. The dynamic pressure was then increased to the desired value at which time the flaps were again excited and the transient decay was recorded. The model was again protected by the wedge and the flow stopped. This procedure was repeated for each test condition. Throughout the tunnel operation, stagnation temperatures and pressures were recorded on an oscillograph together with the output of the model pressure transducers, flap strain gages, and flap actuation signal; this procedure thus allowed the tunnel conditions to be correlated with the model surface-pressure distribution and flap-response data. High-speed continuous schlieren motion pictures were obtained for flow visualization of the tests.

DATA REDUCTION AND ANALYSIS

The experimental damping decrements were reduced to average total aerodynamic coefficients $\overline{N}_5$ and $\overline{N}_6$. All damping terms are assumed to be proportional to amplitude and in phase with velocity. The following equation of equilibrium

$$I_{\alpha,i}\ddot{\theta} + K_{\alpha}\left(1 + ig_{o,i}\right)\theta = -4\rho b^2 V^2 k^2\left(\overline{N}_5 + i\overline{N}_6\right)\theta \tag{1}$$

leads to the following equations (see ref. 5) for the aerodynamic stiffness coefficient

$$\overline{N}_5 = \mu_i r_{\alpha,i}^2 \left[1 - \left(\frac{\omega_{o,i}}{\omega_{t,i}}\right)^2\right] \tag{2}$$

and for the aerodynamic damping coefficient

$$\overline{N}_6 = \mu_i r_{\alpha,i}^2 \left[g_{t,i} - g_{o,i}\left(\frac{\omega_{o,i}}{\omega_{t,i}}\right)^2\right] \tag{3}$$

where

$$\mu_i r_{\alpha,i}^2 = \left(\frac{m_i}{4\rho b^2}\right)\left(\frac{I_{\alpha,i}}{m_i b^2}\right) = \frac{I_{\alpha,i}}{4\rho b^4} \tag{4}$$

is an inertia parameter. To obtain the aforementioned results it has been assumed that the structural damping force is independent of frequency and that the damping values are small.

The experimental-pressure and aerodynamic-coefficient results are compared with theoretical values which were calculated by several methods. The basic method used was Newtonian theory and the other two methods were modifications of Newtonian theory, hereinafter referred to as the "local-wedge correction" and the "local-impact correction." The local-wedge correction assumes that the effective flow along the body follows the separated boundary-layer wedge and, consequently, predicts increased pressures due to boundary-layer separation. The local-impact correction assumes that the free-stream flow has been corrected by a first-order approximation for the viscous effects of the strong bow shock wave. This is accomplished by taking into account the density increase across the normal shock and by describing the local flow parallel to the body surface ahead of the flap. The pressure coefficients are defined by the three methods as follows:

Newtonian theory:

$$C_p = 2 \sin^2\phi \tag{5a}$$

Local-wedge correction:

$$C_p = 2 \sin^2(\phi + \delta) \tag{5b}$$

Local-impact correction:

$$C_p = 2\left(\frac{\rho_l}{\rho_\infty}\right)\left(\frac{V_l}{V_\infty}\right)^2 \sin^2\beta_i \tag{5c}$$

Theoretical pressures were calculated by using Newtonian theory (eq. (5a)) and the local-wedge correction (eq. (5b)) where δ is the separation wedge angle and was measured from schlieren photographs taken during the wind-tunnel tests. The local-wedge

correction is included in an effort to calculate the body surface pressures in the vicinity of the boundary-layer separation ahead of the flaps.

The model-flap unsteady aerodynamic stiffness coefficient $\overline{N}_5$ was calculated by using

$$\overline{N}_5 = \frac{1}{2k_\infty{}^2} \sin 2\phi \tag{6}$$

which was derived in reference 6 by using Newtonian theory. The aerodynamic damping coefficient $\overline{N}_6$ was calculated by using Newtonian theory and local-impact correction. By using Newtonian theory from reference 6, the damping coefficient is

$$\overline{N}_{6,\infty} = \frac{4}{3} \frac{1}{k_\infty} \sin \phi \tag{7}$$

For the local-impact correction, consider the aerodynamic forcing function associated with the moment due to damping as given by part of the right-hand side of equation (1)

$$-4\rho_\infty V_\infty{}^2 b^2 k_\infty{}^2 \left(i\overline{N}_{6,\infty}\right)\theta \tag{8}$$

where the subscript ∞ has been added to denote the usual free-stream characteristics. A similar expression is needed based on local-flow conditions and is obtained by modifying expression (8) by a coefficient A as follows:

$$A\left[-4\rho_\infty V_\infty{}^2 b^2 k_\infty{}^2 \left(i\overline{N}_{6,\infty}\right)\theta\right] = -4\rho_l V_l{}^2 b^2 k_l{}^2 \left(i\overline{N}_{6,l}\right)\theta \tag{9}$$

From equation (9) the modifying coefficient A is determined to be

$$A = \left(\frac{\rho_l}{\rho_\infty}\right)\frac{\overline{N}_{6,l}}{\overline{N}_{6,\infty}} \tag{10}$$

and the local-impact forcing function modifying expression (8) becomes

$$-4\rho_\infty V_\infty{}^2 b^2 k_\infty{}^2 \left[\left(\frac{\rho_l}{\rho_\infty}\right)\left(\frac{\overline{N}_{6,l}}{\overline{N}_{6,\infty}}\right) i\overline{N}_{6,\infty}\right]\theta \tag{11}$$

By recalling the expression for damping coefficient given in equation (7), a similar expression can be defined for the local flow. Thus,

$$\overline{N}_{6,l} = \frac{4}{3} \frac{1}{k_l} \sin \beta_i \tag{12}$$

where β_i is the angle between the local flow and the flap. Therefore,

$$\frac{\overline{N}_{6,l}}{\overline{N}_{6,\infty}} = \left(\frac{k_\infty}{k_l}\right)\frac{\sin \beta_i}{\sin \phi} \tag{13}$$

By substituting the ratio given by equation (13) into expression (11), the local-impact forcing function becomes

$$-4\rho_\infty V_\infty{}^2 b^2 k_\infty{}^2 i\left[\left(\frac{\rho_l}{\rho_\infty}\right)\left(\frac{k_\infty}{k_l}\right)\left(\frac{\sin\beta_i}{\sin\phi}\right)\overline{N}_{6,\infty}\right]\theta \tag{14}$$

where, now for the local-impact correction, the damping coefficient (the term inside the brackets of expression (14)) is

$$\overline{N}_6 = \frac{4}{3}\frac{1}{k_l}\left(\frac{\rho_l}{\rho_\infty}\right)\sin\beta_i = \frac{4}{3}\frac{1}{k_\infty}\left(\frac{V_l}{V_\infty}\right)\left(\frac{\rho_l}{\rho_\infty}\right)\sin\beta_i \tag{15}$$

For the local-impact-correction calculations, equation (15) is used where ρ_l is taken as the density behind a normal shock. (At M = 15.4 in helium, $\rho_l = 3.95\rho_\infty$.) Also, $V_l/V_\infty = \cos\alpha_l$, where α_l is the local-flow angle with respect to the free-stream flow.

RESULTS AND DISCUSSION

Two-Dimensional Configuration

Measured pressure distributions on the blunt two-dimensional configuration at angles of attack of 0^o and 15^o are presented in table III and in figures 6 and 7, respectively. The effect of flap-deflection-angle variation on the magnitude of the pressure ratio p/q measured at various surface locations is illustrated. In general, increasing the flap angle to about 15^o had no visible effect on the pressure distribution. This indicates that if flow separation existed the separation point was located aft of the most rearward pressure cell.

Increasing the flap angle to about 30^o caused a pressure rise immediately ahead of the flap, at the first cell location; and a further increase in flap angle caused pressure rises at more forward locations on the surface. The pressure rises are indicative of the forward motion of the flow-separation point with increasing flap-deflection angle. The pressure distribution generally follows the trend predicted by Newtonian theory for the highly blunted forward portion of the configuration that extends to the region near the shoulder. Measured pressures aft of the shoulder, on the flat surfaces of the configuration, were in all cases higher than the Newtonian values. It is recognized that part of the difference can be attributed to viscous effects which are not accounted for by the theory.

The typical schlieren photographs of figure 8 show the changes in the flow pattern for the blunt two-dimensional configuration at angles of attack of 0^o and 15^o as the flap-deflection angle is varied from 0^o to about 70^o. From the schlieren photographs and the measured pressure distributions, estimates of the separation-point locations and separation-wedge angles were obtained for most of the tests. These data are presented in figures 9 and 10, respectively, as a function of the variation in flap-deflection angle.

Although some scatter is evident in the results, a line faired through the data points indicates a linear trend for both parameters. This result is consistent with the results of reference 3 at $M = 4.5$ to 6 on a sharp-leading-edge two-dimensional model. Values from these faired curves were used in combination with equation (5b) to calculate an empirical pressure distribution over the portion of the model surface where separated flow existed. The resulting pressure distributions are shown in figures 11 and 12 and indicate a reasonable comparison between the measured and calculated trends. It might be noted in these figures that no significant effect is seen of slotted or unslotted flap leading edges on the pressure distributions.

In all cases for the two-dimensional tests, the flaps responded to the excitation in an exponentially decaying manner due to damping. The pressure data from the transducers located ahead of the flaps indicated an unsteady, sinusoidal pressure response corresponding to the flap natural frequency during excitation for flap angles greater than about 15°. Both the pressure and flap response were steady throughout the unexcited portions of the wind-tunnel tests.

The aerodynamic stiffness and damping parameters $k^2\overline{N}_5$ and $k\overline{N}_6$, respectively, were calculated from a comparison of the flap response to a $\pm 1^{\circ}$ instantaneous excitation obtained in both a vacuum and at the test Mach number of 15.4 by the free-oscillation technique. Results for the two-dimensional configuration for a range of flap reduced frequencies and deflection angles are given in table IV and in figures 13 to 16; for the three-dimensional configuration, the results are given in table II and in figures 17 to 19.

In figures 13 to 16, the aerodynamic parameters $k^2\overline{N}_5$ and $k\overline{N}_6$ for the two-dimensional tests are plotted against the reduced frequency $k = b\omega_{t,i}/V$. The comparisons between the experimental values of $k^2\overline{N}_5$ and those calculated by using Newtonian theory show fair agreement as seen in figures 13 and 14. The effect of flap-deflection angle β_i on the aerodynamic parameter $k\overline{N}_6$ is seen in figures 15 and 16. In general, increasing β_i increases $k\overline{N}_6$ for a constant value of reduced frequency. For a given flap-deflection angle, increasing the reduced frequency is seen to lower the value of $k\overline{N}_6$. Comparison between Newtonian theory for the lower flap-deflection angles and local-impact correction for the higher angles, with the experimental damping results, shows, in general, good agreement.

Three-Dimensional Configuration

A representative reentry-vehicle model was used to investigate the influence of a number of parameters associated with three-dimensional flow on flap response. The typical schlieren photographs of figure 17 show the changes in the flow pattern for the three-dimensional configuration at angles of attack of 0° and 25° as the flap-deflection angle is varied from 0° to about 60°. The schlieren photographs indicate no visible flow

separation for the model at zero angle of attack (fig. 17(a)) over the range of flap-deflection angles tested. With the model at an angle of attack of 25°, as the flap angle increases (figs. 17(b), 17(c), and 17(d)), the separated-flow region also increases with subsequent movement of the reattachment shock toward the trailing edge of the flap. Also shown in figures 17(b), 17(c), and 17(d) are the bow shock, flap shocks, and the shock from the separation wedge intersecting to form a multiple set of shocks which, for increasing flap angles, is seen to be moving upstream. For flap angles greater than 30° this multiple set of shocks was observed to be unsteady in the vicinity of the flap and, as β_i was increased to larger angles, became more violent and influenced the shocks further upstream. This unsteady response was also measured on the model flaps for the same flap angles during the tests, and the amplitude of the response increased with increasing flap angle. In all cases, the flap response was random in nature and nondivergent.

Comparisons between the measured results and calculations using Newtonian theory are shown in figures 18 and 19 for both the stiffness and damping parameters $k^2\overline{N}_5$ and $k\overline{N}_6$, respectively. In figure 18 the aerodynamic-stiffness results are presented as a function of flap-deflection angle for the body at angles of attack of 0° and 25°. No discernible trends of measured $k^2\overline{N}_5$ can be seen and, consequently, no meaningful comparisons can be made. In figure 19 the aerodynamic-damping results are presented as a function of flap angle for the body at angles of attack of 0° and 25°. The measured results are shown in a band which illustrates a decreasing trend of aerodynamic damping with increasing flap angle for the body at both angles of attack. Special attention is called to the measured negative damping values shown in figure 19(b) for the model at $\alpha = 25^{\circ}$ and to flap angles greater than about 37°. Since the theory predicted a stabilizing trend of increasing amounts of damping for increasing flap angles, the measured flap response was not predicted and the theory was, therefore, judged inadequate. Local-impact correction, although not shown, would not change the predicted trends, only their magnitudes. It is useful to examine the practical implications of the measured unstable-damping values shown in figure 19(b).

Generally, there are two basic governing parameters needed to simulate the aeroelastic properties of vehicles in addition to the obvious one of Mach number. They are the inertia and frequency parameters. In order to relate the test results of the 1/30-scale model of this investigation to flight-vehicle conditions, an approximate relationship for the aerodynamic damping coefficient obtained from equation (3) can be used. Therefore,

$$g_a \approx \frac{\overline{N}_6}{\mu_i r_{\alpha,i}^2}$$

where $\omega_{o,i}/\omega_{t,i}$ has been assumed approximately equal to 1.

Attention is again called to figure 1 which presents a typical aeroelastic corridor for a reentry flap flying at $M = 15$. It is pointed out that for aeroelastic considerations the most stringent design criteria at this Mach number would be associated with the inertia and frequency values at the lower left-hand corner of the boundary. By selecting the value of $\mu_i r_{\alpha,i}^2$ of 1.25×10^4 from figure 1, values of aerodynamic damping for a full-scale vehicle could be evaluated for the flap-deflection angles which indicated negative values of aerodynamic damping. The values of g_a predicted from the model results are: -0.0038, -0.0046, and -0.0054 for flap-deflection angles of 40^o, 50^o, and 58^o, respectively. These values are sufficiently small that they would not be expected to be large enough to overcome the normal amount of structural damping expected to be present for a practical design.

The implication of the previous discussion is that the configuration would not encounter a divergent instability within its flight regime and, therefore, would not be a prime design problem. It should be noted, however, that the present investigation was of limited scope for one configuration, and, since the experimental results were not predicted, future work should be undertaken as new configurations evolve.

CONCLUSIONS

An experimental investigation was conducted in helium flow at a Mach number M of 15.4 and a Reynolds number range per meter from 23.0×10^6 to 26.2×10^6 (7×10^6 to 8×10^6 per foot) to obtain information on flap behavior over a selected range of aeroelastic parameters.

Two-Dimensional Configuration

The results for control-surface flaps mounted on a blunt two-dimensional configuration at angles of attack α of 0^o and 15^o indicated the following conclusions:

1. A separated flow region ahead of the flaps increased in size with increasing flap-deflection angle and caused local surface pressures to increase. These increased pressures were calculated with reasonable accuracy.

2. Measured aerodynamic stiffness and damping coefficients were, in general, stabilizing. A trend of increasing amounts of damping with increasing flap-deflection angles (from 0^o to 70^o) was exhibited. Comparison between calculated and experimental results showed good agreement.

Three-Dimensional Configuration

Results of studies conducted with control-surface flaps mounted on a 1/30-scale three-dimensional model of a representative reentry vehicle at angle of attack of 0^o and 25^o indicated the following conclusions:

1. A multiple set of shocks intersected off, but in the vicinity of, the flap trailing edge. When the model was at an angle of attack of 25°, this multiple set of shocks was observed to be unsteady for flap angles greater than about 30°, and the shocks became more violent for larger flap angles.

2. With the model at $\alpha = 25^{\circ}$, the flap response was also unsteady for flap angles greater than about 30° and the amplitude of the response increased with increasing flap angles. The response observed was random and nondivergent.

3. A destabilizing trend of aerodynamic damping was measured with respect to increasing flap angles which was not predicted by theory. Negative damping was measured for flap angles greater than about 37°. The exact cause of the unstable aerodynamic damping was not determined.

4. Although the present results do not indicate an immediate problem for the designer, future investigations should be undertaken as new configurations evolve.

Langley Research Center,
National Aeronautics and Space Administration,
Hampton, Va., June 7, 1971.

REFERENCES

1. Widmayer, E.: Aerodynamic Excitation of Flaps at M = 16. Rep. No. 202S-38, Martin Co., Sept. 22, 1961.

2. Widmayer, Edward, Jr.: Preliminary Investigation of the Aerodynamic Excitation of Flaps at Hypersonic Speeds. RM-159, Martin Marietta Corp., Aug. 1963.

3. Goldman, R. L.; Morkovin, M. V.; and Schumacher, R. N.: Unsteady Control Surface Loads of Lifting Re-Entry Vehicles at Very High Speeds. AIAA J., vol. 6, no. 1, Jan. 1968, pp. 44-50.

4. Goetz, Robert C.: Effects of Leading-Edge Bluntness on Flutter Characteristics of Some Square-Planform Double-Wedge Airfoils at a Mach Number of 15.4. NASA TN D-1487, 1962.

5. Widmayer, Edward, Jr.; Clevenson, Sherman A.; and Leadbetter, Sumner A.: Some Measurements of Aerodynamic Forces and Moments at Subsonic Speeds on a Rectangular Wing of Aspect Ratio 2 Oscillating About the Midchord. NASA TN 4240, 1958. (Supersedes NACA RM L53F19.)

6. Hall, B. M.; and Martin, E. N.: Newtonian Oscillatory Aerodynamic Coefficients. Paper No. 3885, Missile & Space Systems Div., Douglas Aircraft Co., Inc., Mar. 1966.

TABLE I.- CONTROL-SURFACE PHYSICAL PARAMETERS OF TWO-DIMENSIONAL MODEL

[b = 0.01102 m (0.036145 ft); S = 0.10796 m (0.3542 ft)]

Test run	β_u, deg	β_L, deg	m_u, kg/m	m_u, slugs/ft	m_L, kg/m	m_L, slugs/ft	$I_{\alpha,u}$, kg-m	$I_{\alpha,u}$, slug-ft	$I_{\alpha,L}$, kg-m	$I_{\alpha,L}$, slug-ft	$r_{\alpha,u}^2$	$r_{\alpha,L}^2$	$\omega_{o,u}$, rad/sec	$\omega_{o,L}$, rad/sec	$g_{o,u}$	$g_{o,L}$
6	0	0	0.06016	12.5637×10^{-4}	0.05772	12.0555×10^{-4}	9.7242×10^{-6}	2.1861×10^{-6}	9.3310×10^{-6}	2.0977×10^{-6}	1.3323	1.3323	3770	2620	0.01474	0.01163
76	0	0	.17100	35.7147	.08449	17.6456	64.2676	14.4480	22.3117	5.0159	3.0975	2.1765	1150	1928	.01425	.00762
75	0	0	.08449	17.6456	.17100	35.7147	22.3117	5.0159	64.2676	14.4480	2.1765	3.0975	1835	1194	.00690	.01380
51	0	15	.08449	17.6456	.17100	35.7147	22.3117	5.0159	64.2676	14.4480	2.1765	3.0975	1841	1194	.00614	.00632
56	0	30	.16641	34.7548	.07989	16.6857	68.4405	15.3861	21.5680	4.8487	3.2099	2.2250	1684	1445	.00818	.00480
67	0	60	.09003	18.8032	.17573	36.7029	26.4850	5.9541	68.4405	15.3861	2.4246	3.2099	2746	1696	.01297	.01005
2	13	13	.06016	12.5637	.05772	12.0555	9.7242	2.1861	9.3310	2.0977	1.3323	1.3323	3858	2639	.01078	.00775
77	14	15	.17100	35.7147	.08449	17.6456	64.2676	14.4480	22.3117	5.0159	3.0975	2.1765	1137	1916	.01104	.00737
78	15	15	.08449	17.6456	.17100	35.7147	22.3117	5.0159	64.2676	14.4480	2.1765	3.0975	1828	1219	.00737	.01380
55	19	33	.08449	17.6456	.05542	11.5755	22.3117	5.0159	8.9591	2.0141	2.1765	1.3323	1759	1407	.00597	.00409
65	15	60	.16641	34.7548	.07989	16.6857	63.5239	14.2808	21.5680	4.8487	3.1463	2.2250	1866	3016	.01472	.01050
74	27	23	.08449	17.6456	.17100	35.7147	22.3117	5.0159	64.2676	14.4480	2.1765	3.0975		1206		.01840
3	27	30	.06016	12.5637	.05772	12.0555	9.7242	2.1861	9.3310	2.0977	1.3323	1.3323	3695	2633	.01381	.00982
64	28	35	.16641	34.7548	.07989	16.6857	63.5239	14.2808	21.5680	4.8487	3.1463	2.2250	1885	3142	.01578	.01228
59	20	42	.16641	34.7548	.07989	16.6857	22.3117	5.0159	64.2676	14.4480	2.1765	3.0975	1835	1062	.00614	.01425
61	24	45	.09033	18.8032	.17573	36.7029	26.4850	5.9541	68.4405	15.3861	2.4246	3.2099	2633	1796	.01300	.01300
60	30	60	.08449	17.6456	.17100	35.7147	22.3117	5.0159	64.2676	14.4480	2.1765	3.0975	1835	1211	.00763	.00763
4	41	43	.06016	12.5637	.05772	12.0555	9.7242	2.1861	9.3310	2.0977	1.3323	1.3323	3886	2617	.01052	.01052
73	46	0	.06641	34.7548	.07989	16.6857	63.5239	14.2808	21.5680	4.8487	3.1463	2.2250	1659	2959	.01340	.00597
5	41	60	.05772	12.0555	.06003	12.5368	9.3310	2.0977	9.7242	2.1861	1.3323	1.3323	2620	3852	.01227	.00941
79	57	59	.08449	17.6456	.17100	35.7147	22.3117	5.0159	64.2676	14.4480	2.1765	3.0975	1998	1049	.01052	.00961
85	55	60	.17100	35.7147	.08449	17.6456	64.2676	14.4480	22.3117	5.0159	3.0975	2.1765	1311	2066	.00789	.01004
72	57	0	.08496	17.7444	.17148	35.8136	23.9931	5.3939	65.9490	14.8260	2.3275	3.1698	2670	1828	.01300	.00850
68	57	20	.17655	36.8723	.09003	18.8032	68.4405	15.3861	26.4850	5.9541	3.1951	2.4246	1690	2853	.01105	.01227
7	0	17	.07989	16.6850	.16640	34.7540	21.5675	4.8486	63.5230	14.2806	2.2250	3.1463	2827	1806	.00451	.00471
26	0	20	.08448	17.6450	.17100	35.7140	22.3331	5.0207	64.2658	14.4476	2.1787	3.0976	1780	1164	.00574	.00497
31	0	16	.08448	17.6450	.17100	35.7140	22.3331	5.0207	64.2658	14.4476	2.1787	3.0976	1860	1204	.00481	.00582
8	1	16	.07989	16.6850	.16640	34.7540	21.5675	4.8486	63.5230	14.2806	2.2250	3.1463	2827	1796	.00452	.00650
10	2	19	.08448	17.6450	.17100	35.7140	22.3331	5.0207	64.2658	14.4476	2.1787	3.0976	2011	1167	.00514	.00539
28	14	18	.07989	16.6850	.16640	34.7540	21.5675	4.8486	63.5230	14.2806	2.2250	3.1463	3245	1989	.00921	.00632
30	15	15	.08448	17.6450	.17100	35.7140	22.3331	5.0207	64.2658	14.4476	2.1787	3.0976	1859	1199	.00481	.00614
12	14	29	.08448	17.6450	.17100	35.7140	22.3331	5.0207	64.2658	14.4476	2.1787	3.0976	1816	1200	.00425	.00632
23	14	29	.08448	17.6450	.17100	35.7140	22.3331	5.0207	64.2658	14.4476	2.1787	3.0976	1857	1208	.00567	.00597
24	15	30	.07989	16.6850	.16640	34.7540	21.5675	4.8486	63.5230	14.2806	2.2250	3.1463	3179	1991	.00884	.00737
11	15	30	.07989	16.6850	.16640	34.7540	21.5675	4.8486	63.5230	14.2806	2.2250	3.1463	2827	1806	.00567	.00691
13	30	45	.07989	16.6850	.16640	34.7540	21.5675	4.8486	63.5230	14.2806	2.2250	3.1463	3142	1863	.01425	.00884
21	35	42	.08692	18.1540	.17343	36.2220	22.7041	5.1041	64.6590	14.5360	2.1528	3.0728	2725	1696	.00737	.01164
22	30	45	.07989	16.6850	.16640	34.7540	21.5675	4.8486	63.5230	14.2806	2.2250	3.1463	3142	1986	.01105	.00632
15	44	61	.07989	16.6850	.16640	34.7540	21.5675	4.8486	63.5230	14.2806	2.2250	3.1463	3091	1822	.00713	.00819
16	46	59	.08692	18.1540	.17343	36.2220	22.7041	5.1041	64.6590	14.5360	2.1528	3.0728	2694	1583	.00539	.00921
17	57	73	.07989	16.6850	.16640	34.7540	21.5675	4.8486	63.5230	14.2806	2.2250	3.1463	3016	1796	.00819	.01381

TABLE II.- EXPERIMENTAL UNSTEADY AERODYNAMIC-COEFFICIENT DATA FOR THREE-DIMENSIONAL CONFIGURATION

[Flow properties: V = 1828.8 m/sec ± 18.29 m/sec (6000 ft/sec ± 60 ft/sec); a = 118.87 m/sec ± 1.189 m/sec (390 ft/sec ± 3.9 ft/sec); M = 15.4
Model properties: b = 0.0127 m (0.04166 ft); S = 0.0343 m (0.1125 ft); $I_\alpha = 25.9775 \times 10^{-6}$ kg-m (5.840 × 10^{-6} slug-ft)]

Test run	α, deg	β_s, deg	β_p, deg	$\omega_{o,s}$, rad/sec	$\omega_{o,p}$, rad/sec	$g_{o,s}$	$g_{o,p}$	q, N/m^2	q, lb/ft^2	ρ, kg/m^3	ρ, $slugs/ft^3$	$\omega_{t,s}$, rad/sec	$\omega_{t,p}$, rad/sec	$g_{t,s}$	$g_{t,p}$	$\mu r_{\alpha,i}^2$	k_s	k_p	$\bar{N}_{5,s}$	$\bar{N}_{5,p}$	$\bar{N}_{6,s}$	$\bar{N}_{6,p}$
33	0	15	15	237.5	320.0	0.00631	0.01480	13 167	275	0.0079	1.530×10^{-5}	242.9	324.9		0.01579	5.5×10^4	0.0106	0.0142		1650		78.6
34	25	15	15	235.8	314.2	.00606	.01634	21 977	459	.0131	2.550	245.5	328.6		.01700	3.295	.0107	.0143		2830		68.2
36	0	23	24.5	257.2	400.0	.00631	.00650	22 264	465	.0133	2.585	259.0	410.0	0.00790	.00713	3.254	.0113	.0179	456	1568	54.7	30.6
37	25	17	19	260.0	400.0	.01004	.00690	23 653	494	.0141	2.745	265.7	424.0	.01378	.00884	3.060	.0116	.0185	1301	3372	127.6	82.6
38	25	32	35	262.5	404.5	.00566	.00650	12 209	255	.0073	1.417	268.5	414.2	.00580		5.925	.0117	.0181	2625		23.1	
39	0	36.5	40.5	282.4	405.0	.00606	.00650	21 648	452	.0129	2.510	266.7	408.1	.00622	.00680	3.345	.0116	.0178	1074	505	11.7	13.4
40	25	40	36	700.0	408.0	.01262	.00775	23 772	496.5	.0142	2.760	700.0	417.0	.01105	.00790	3.044	.0305	.0182	0	1300	-47.8	14.6
47	25	50	58	360.0	880.0	.00691	.01052	23 749	496	.0142	2.760	363.0	885.0	.00489	.00818	3.044	.0158	.0386	502	347	-57.8	-67.6

TABLE III.- EXPERIMENTAL PRESSURE DISTRIBUTION ON TWO-DIMENSIONAL CONFIGURATION

(a) $\alpha = 0^o$

Test run	Model flap angle		Free-stream conditions								Local pressure, fraction of dynamic pressure										
											Lower surface gage location						Upper surface gage location				
	β_u, deg	β_L, deg	q, N/m^2	q, lb/ft^2	a, m/sec	a, ft/sec	ρ, kg/m^3	ρ, $slugs/ft^3$	V, m/sec	V, ft/sec	1	2	3	4	5	6	7	8	9	10	1
6	0	0	2.490×10^4	520	117.6	385.7	0.0152	2.947×10^{-5}	1810	5940	1.76	1.62	0.86	0.46	0.12	0.08	0.65	0.71	0.70	1.58	1.76
76	0	0	2.083	435	120.7	396.1	.0119	2.315	1859	6099	1.95			.51	.11	.10	.68	.75		1.62	1.95
75	0	0	1.848	386	118.5	388.8	.0110	2.142	1813	5948	1.98			.49	.10	.10	.68	.77		1.64	1.98
51	0	15	2.346	490	119.0	390.5	.0142	2.754	1833	6013	1.72			.42	.11	.08	.68			1.63	1.72
56	0	30	2.380	497	118.4	388.3	.0148	2.881	1823	5980	1.85			.46	.14	.12	.64	.71		1.62	1.85
67	0	60	2.245	469	119.3	391.4	.0140	2.714	1837	6027	1.86			.54		.37	.67	.73		1.68	1.86
2	13	13	2.648	553	118.2	387.9	.0160	3.099	1821	5974	1.79	1.61	.84	.46	.11	.08	.68	.77	.75	1.60	1.79
77	14	15	2.006	419	120.3	394.6	.0115	2.239	1840	6036	1.89			.52	.09	.11	.73	.77		1.61	1.89
78	15	15	2.346	490	119.5	392.2	.0138	2.683	1840	6038	1.84			.51	.11	.11	.74	.77		1.66	1.84
55	19	33	2.360	493	119.8	393.1	.0138	2.682	1846	6055	1.83			.48			.80	.75		1.62	1.83
65	15	60	2.394	500	118.7	389.5	.0134	2.600	1829	6000	1.81			.56	.37	.30	.72	.74		1.61	1.81
74	27	23	1.977	413	118.2	387.9	.0121	2.344	1809	5935	1.93			.53	.09	.08	.84	.79		1.62	1.93
3	27	30	2.490	520	118.3	388.2	.0148	2.876	1822	5978	1.80	1.56	.83	.45	.12	.12	.83	.82	.75	1.61	1.80
64	28	35	2.394	500	119.3	391.4	.0137	2.654	1837	6027	1.77			.48	.11	.13	.82	.78		1.63	1.77
59	20	42	2.068	432	119.8	393.2	.0111	2.154	1846	6055	1.81			.48	.28	.21	.81	.80		1.65	1.81
61	24	45	2.159	451	120.0	393.7	.0127	2.462	1848	6063	1.84			.50	.30	.25	.85	.79		1.61	1.84
60	30	60	2.011	420	118.4	388.3	.0120	2.336	1811	5940	1.82			.47	.44	.32	.86	.85		1.63	1.82
4	41	43	2.475	517	119.8	393.2	.0145	2.820	1846	6055	1.90	1.58	.84	.43	.29	.17	1.01	1.11	.73	1.56	1.90
73	46	0	2.159	451	118.5	388.8	.0129	2.498	1825	5988	1.94			.52	.11	.09	1.36	1.12		1.71	1.94
5	41	60	2.518	526	119.1	390.6	.0150	2.907	1834	6016	1.75	1.54	1.06	.42	.44	.27	1.01	1.17	.76	1.57	1.75
79	57	59	2.140	447	119.9	393.3	.0125	2.435	1846	6058	1.93			.59	.47	.33	1.55	1.55		1.70	1.93
85	55	60	2.375	496	119.5	391.9	.0140	2.724	1840	6036				.57	.50	.39	1.53	1.49		1.70	
72	57	0	2.040	426	119.4	391.8	.0120	2.327	1827	5993	1.96			.43	.10	.09	1.53	1.36		1.72	1.96
68	57	20	2.332	487	120.7	396.1	.0126	2.454	1859	6099	1.83			.54	.10	.09	1.51	1.43		1.73	1.83

TABLE III.- EXPERIMENTAL PRESSURE DISTRIBUTION ON TWO-DIMENSIONAL CONFIGURATION – Concluded

(b) $\alpha = 15^{o}$

Test run	Model flap angle		Free-stream conditions								Local pressure, fraction of dynamic pressure										
											Lower surface gage location					Upper surface gage location					
	β_u, deg	β_L, deg	q, N/m^2	q, lb/ft^2	a, m/sec	a, ft/sec	ρ, kg/m^3	ρ, $slugs/ft^3$	V, m/sec	V, ft/sec	2	3	4	5	6	7	8	9	10	1	2
7	0	17	2.542×10^4	531	120.3	394.6	0.0148	2.876×10^{-5}	1852	6077	1.78	1.20	0.68	0.28	0.20	0.28	0.27	0.33	1.24	1.72	1.78
8	1	16	2.471	516	120.3	394.8	.0144	2.791	1853	6081	1.80	1.24	.77	.29	.22	.29	.29	.34	1.28	1.78	1.80
10	2	19	2.380	497	119.6	392.4	.0140	2.722	1842	6043	1.80	1.16	.775	.295	.29	.30	.29	.35	1.26	1.75	1.80
31	0	16	2.605	544	120.5	395.3	.0151	2.932	1854	6088	1.82			.31	.26	.30	.30				1.82
29	0	23	2.576	538	120.7	396.1	.0149	2.892	1859	6100	1.78			.33	.24	.33	.30				1.78
26	0	20	2.490	520	120.0	393.6	.0146	2.830	1847	6061	1.76			.28	.20	.28	.27				1.76
28	14	18	2.538	530	120.0	393.8	.0149	2.882	1849	6065	1.75			.29	.25	.255	.25				1.75
30	15	15	2.538	530	119.5	392.2	.0150	2.906	1841	6039	1.78			.28	.24	.34	.27				1.78
11	15	30	2.365	494	119.6	392.4	.0139	2.705	1842	6043	1.85	1.25	.76	.29	.33	.30	.34	.385	1.24	1.79	1.85
12	14	29	2.518	526	118.6	389.2	.0151	2.925	1827	5994	1.88	1.29	.77	.37	.39	.32	.35	.40	1.31	1.85	1.88
23	14	29	2.547	532	118.7	389.5	.0152	2.957	1828	5998	1.86			.345	.40	.33	.32				1.86
24	15	30	2.586	540	119.5	392.2	.0153	2.961	1841	6039	1.82			.30	.34	.34	.28				1.82
13	30	45	2.595	542	119.2	391.1	.0154	2.987	1836	6024	1.85	1.29	.77	.60	.46	.35	.35	.40	1.29	1.81	1.85
14	32	42	2.586	540	118.7	389.5	.0155	3.002	1828	5998	1.85	1.31	.76	.71	.565	.41	.42	.40	1.31	1.83	1.85
21	35	42	2.480	518	119.5	392.2	.0146	2.840	1841	6039	1.81			.66	.50	.51					1.81
22	30	45	2.564	535.5	119.1	390.9	.0152	2.955	1835	6020	1.87			.59	.54	.42	.31				1.87
19	30	75	2.509	524	120.3	394.6	.0146	2.838	1853	6081	1.81	1.22	.71	1.08	.96	.40	.40	.38	1.325	1.765	1.81
15	44	61	2.471	516	121.8	399.7	.0140	2.724	1876	6156	1.83	1.24	.77	.81	.73	.52	.56	.36	1.27	1.78	1.83
16	46	59	2.562	535	119.2	391.1	.0152	2.949	1836	6024	1.87	1.26	.82	.96	.79	.60	.59	.51	1.30	1.80	1.87
17	57	73	2.566	536	120.8	396.4	.0148	2.877	1860	6104	1.87	1.24	.82	.97	.87	.64	.645	.575	1.24	1.81	1.87

TABLE IV.- EXPERIMENTAL UNSTEADY AERODYNAMIC-COEFFICIENT DATA

FOR TWO-DIMENSIONAL CONFIGURATION

(a) $\alpha = 0^{o}$

Test run	β_u, deg	β_L, deg	μ_u	μ_L	$\omega_{t,u}$, rad/sec	$\omega_{t,L}$, rad/sec	$g_{t,u}$	$g_{t,L}$	k_u	k_L	$\overline{N}_{5,u}$	$\overline{N}_{5,L}$	$\overline{N}_{6,u}$	$\overline{N}_{6,L}$
6	0	0	8 161	7 832										
76	0	0	29 533	14 592	1200	1928	0.01444	0.00884	0.00711	0.01143	7 460	0	124.0	38.8
75	0	0	15 770	31 919	1923	1200	.00650	.01467	.01168	.00729	3 068	989	7.6	100.5
51	0	15	12 266	24 826	1973	1213	.00819	.00885	.01186	.00729	3 452	2399	68.9	210.0
56	0	30	24 395	11 086	1634	1464	.00980	.02010	.00988	.00885	4 863	636	74.7	379.0
67	0	60	13 261	25 888	2796	1822	.01402	.01427	.01677	.01093			48.5	462.1
2	13	13	7 761	7 448										
77	14	15	30 536	15 087	1206	1948	.01268	.01004	.00722	.01166	10 510	1074	271.5	95.2
78	15	15	12 590	25 483	1960	1216	.00960	.01654	.01173	.00728	3 570	-379	87.1	213.9
55	19	33	12 595	8 262	1854	1571	.01238	.02760	.01107	.00938	2 736	218	192.2	267.7
65	15	60	25 588	12 285	1948	3142	.01300	.01840	.01173	.01893	6 634	2154	-40.9	238.3
74	27	23	14 411	29 168		1244		.02207		.00758		5448		431.9
3	27	30	8 362	8 025										
64	28	35	25 068	12 035	1885	3142	.01922	.01841	.01130	.01884	0	0	271.2	164.2
59	20	42	30 887	14 828		1049		.03422		.00626		1139		900.7
61	24	45	14 618	28 538	2683	1800	.01755	.01718	.01599	.01073	1 315	3142	178.3	388.4
60	30	60	14 461	29 268	1885	1225	.01578	.01841	.01147	.00745	1 652	2076	269.4	992.8
4	41	43	8 528	8 184										
73	46	0	26 633	12 786	1684	2959	.01776	.00670	.01016	.01786	2 480	0	398.9	20.7
5	41	60	7 939	8 255										
79	57	59	7 939	8 273	2011	1068	.03087	.06887	.9110	.00637	225	905	354.1	1527.0
85	55	60	13 873	28 078	1307	2092	.02832	.01472	.00783	.01253	-257	1516	877.1	300.7
72	57	0	25 099	12 401	2783	1841	.01608	.00920	.01678	.01110	4 656	554	240.1	32.2
68	57	20	14 598	29 459	1696	2853	.02460	.01318	.01005	.01691	336	0	636.2	65.0

TABLE IV.- EXPERIMENTAL UNSTEADY AERODYNAMIC-COEFFICIENT DATA

FOR TWO-DIMENSIONAL CONFIGURATION – Concluded

(b) $\alpha = 15^{o}$

Test run	β_u, deg	β_L, deg	μ_u	μ_L	$\omega_{t,u}$, rad/sec	$\omega_{t,L}$, rad/sec	$g_{t,u}$	$g_{t,L}$	k_u	k_L	$\overline{N}_{5,u}$	$\overline{N}_{5,L}$	$\overline{N}_{6,u}$	$\overline{N}_{6,L}$
7	0	17	11 106	23 132	2827	1822	0.00553	0.00640	0.01682	0.01084	0	1274	25.2	128.8
8	1	16	11 444	23 837	2865	1838	.00582	.00526	.01704	.01092	672	3397	36.4	-71.2
10	2	19	12 409	25 115	2061	1236	.00574	.00750	.01233	.00740	1159	8456	23.0	210.0
31	0	16	11 520	23 317	1925	1275	.00402	.00713	.01143	.00757			-12.0	139.4
29	0	23												
26	0	20	11 935	24 157	1847	1188	.00850	.00932	.01102	.00708			82.4	339.7
28	14	18	11 082	23 083	3299	2042	.01228	.00748	.01965	.01217	801	3727	82.8	107.5
30	15	15	11 623	23 525	2024	1242	.00597	.00762	.01212	.00744	3961	4970	48.6	137.7
11	15	30	11 807	24 594	2906	1816	.00598	.01381	.01738	.01086	1411	867	16.0	539.3
12	14	29	11 548	23 373	1948	1218	.00713	.01700	.01175	.00734	3296	2129	86.5	786.3
23	14	29	11 421	23 116	1974	1230	.00481	.01637	.01190	.00742	2864	2542	-5.2	759.7
24	15	30	10 787	22 468	3267	2011	.01052	.01340	.01956	.01204	1279	1407	51.6	436.9
13	30	45	10 691	22 268	3142	1863	.02210	.01768	.01886	.01117	0	0	186.7	619.3
14	32	42												
21	35	42	12 236	24 415	2749	1728	.01637	.01994	.01646	.01035	461	2768	240.5	654.2
22	30	45	10 808	22 513	3204	2004	.01776	.01371	.01924	.01203	923	1268	171.7	531.2
19	30	75												
15	44	61	11 725	24 423	3211	1835	.01694	.01700	.01886	.01077	1915	1083	269.5	685.4
16	46	59	11 784	23 512	2723	1607	.01807	.01922	.01633	.00964	540	2153	324.5	742.7
17	57	73	11 102	23 125	3098	1885	.02455	.02763	.01835	.01116	1292	6723	414.7	1097.9

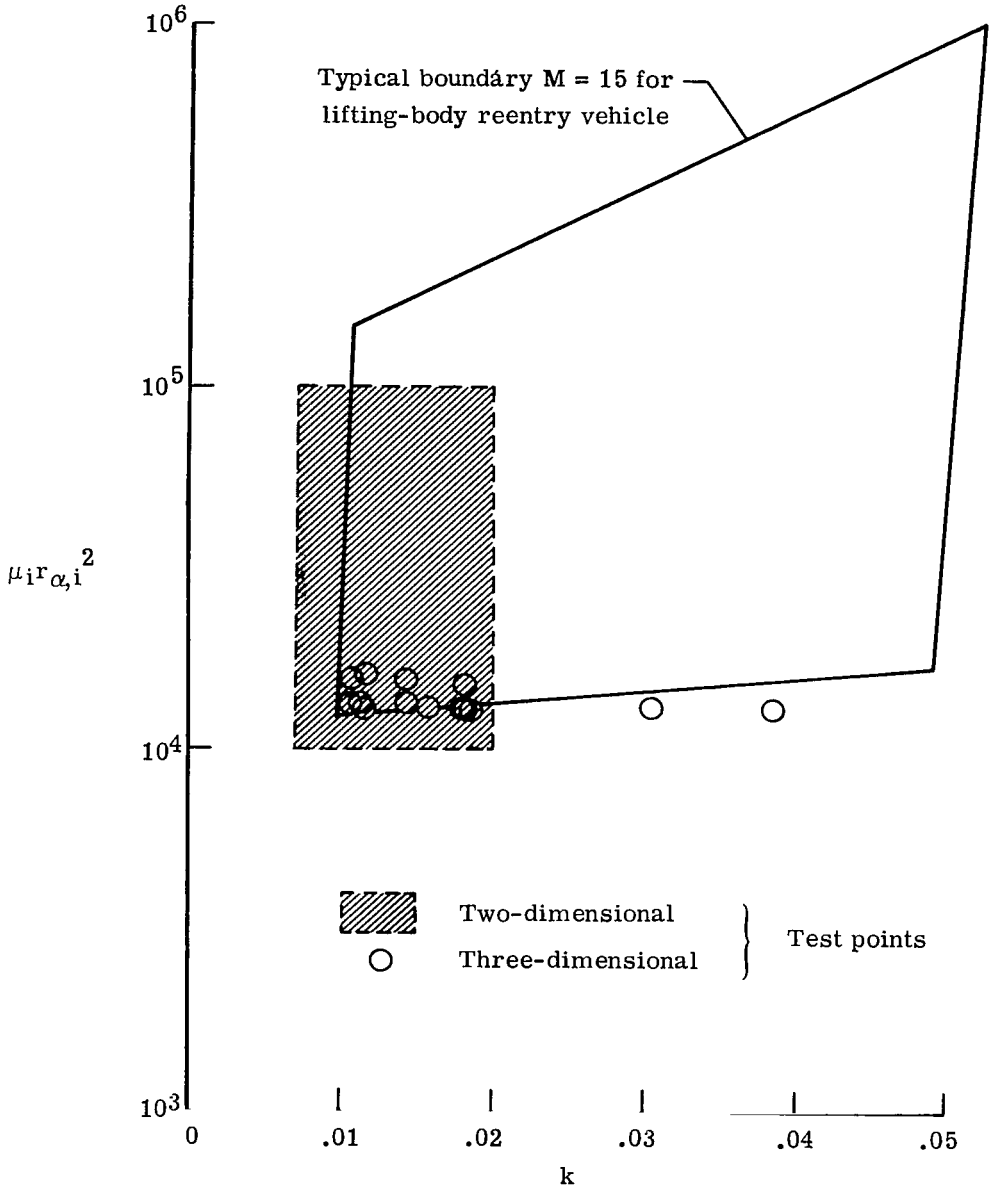

Figure 1.- Aeroelastic parameter corridor.

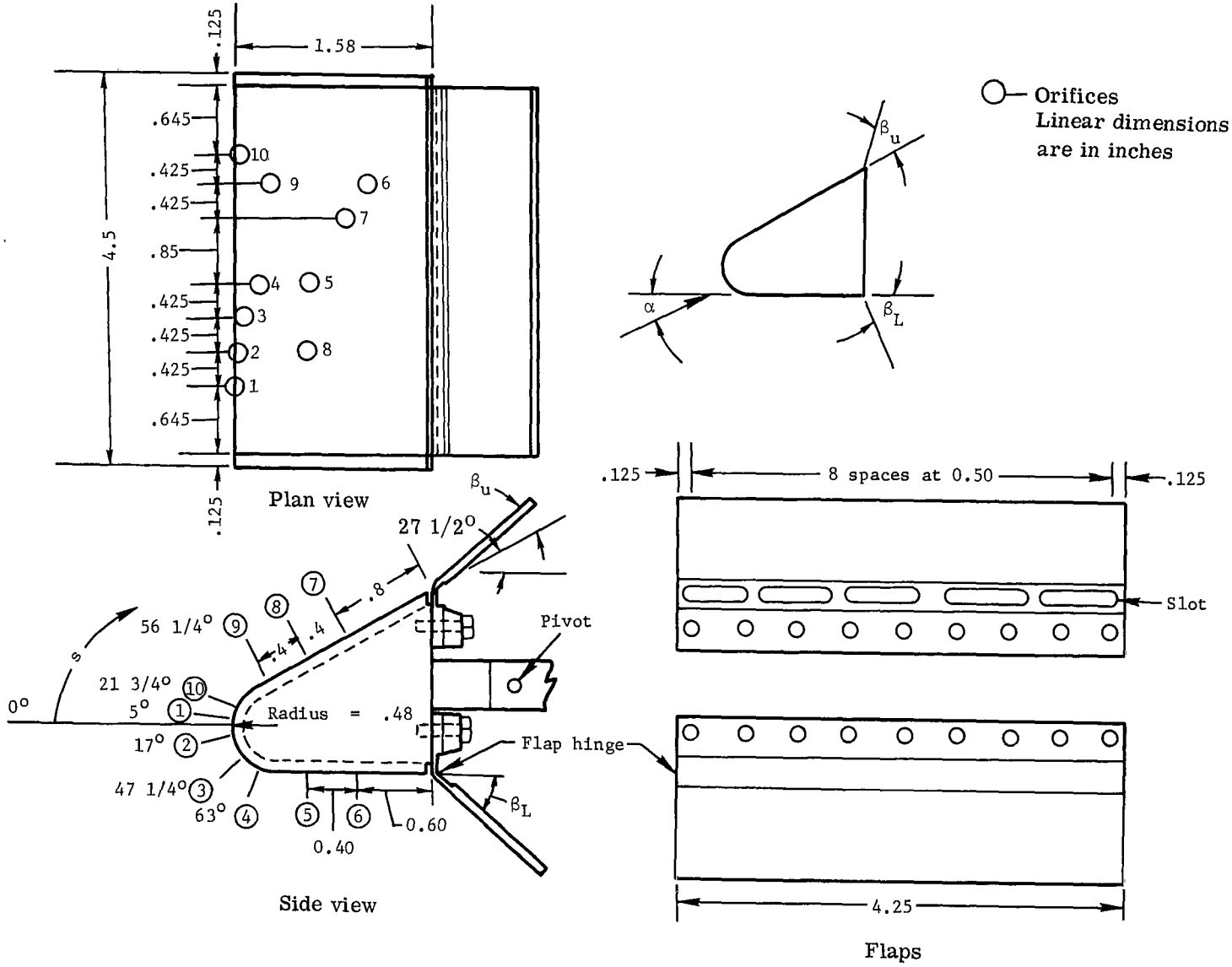

Figure 2.- Sketch of two-dimensional model showing pertinent dimensions and locations of pressure orifices. Linear dimensions are in inches.

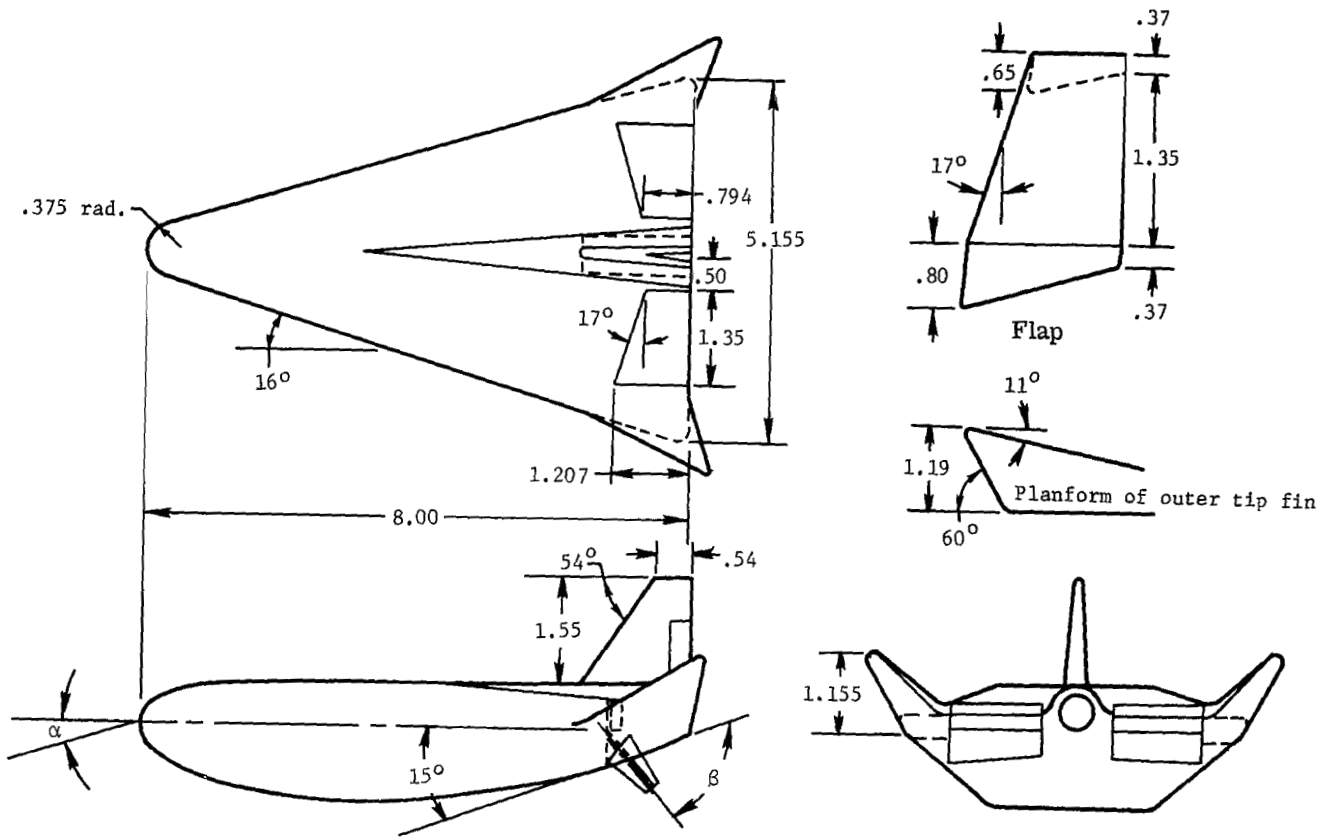

Flap shown deflected in side view only

Figure 3.- Sketch of three-dimensional model showing pertinent dimensions and features. Linear dimensions are in inches.

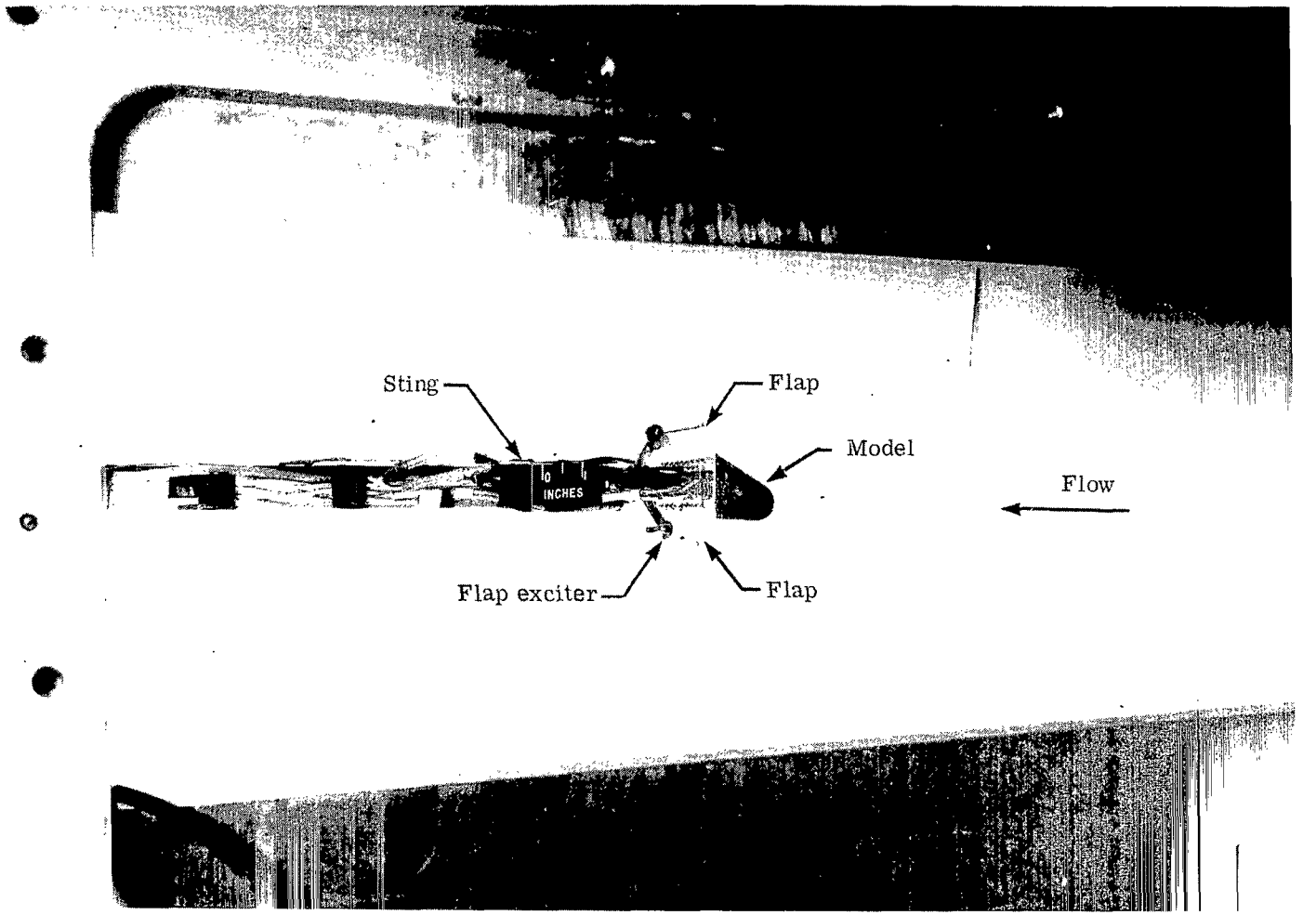

L-66-3132.1

(a) Model with flap-exciter mechanism installed on the sting.

Figure 4.- Photographs of two-dimensional model.

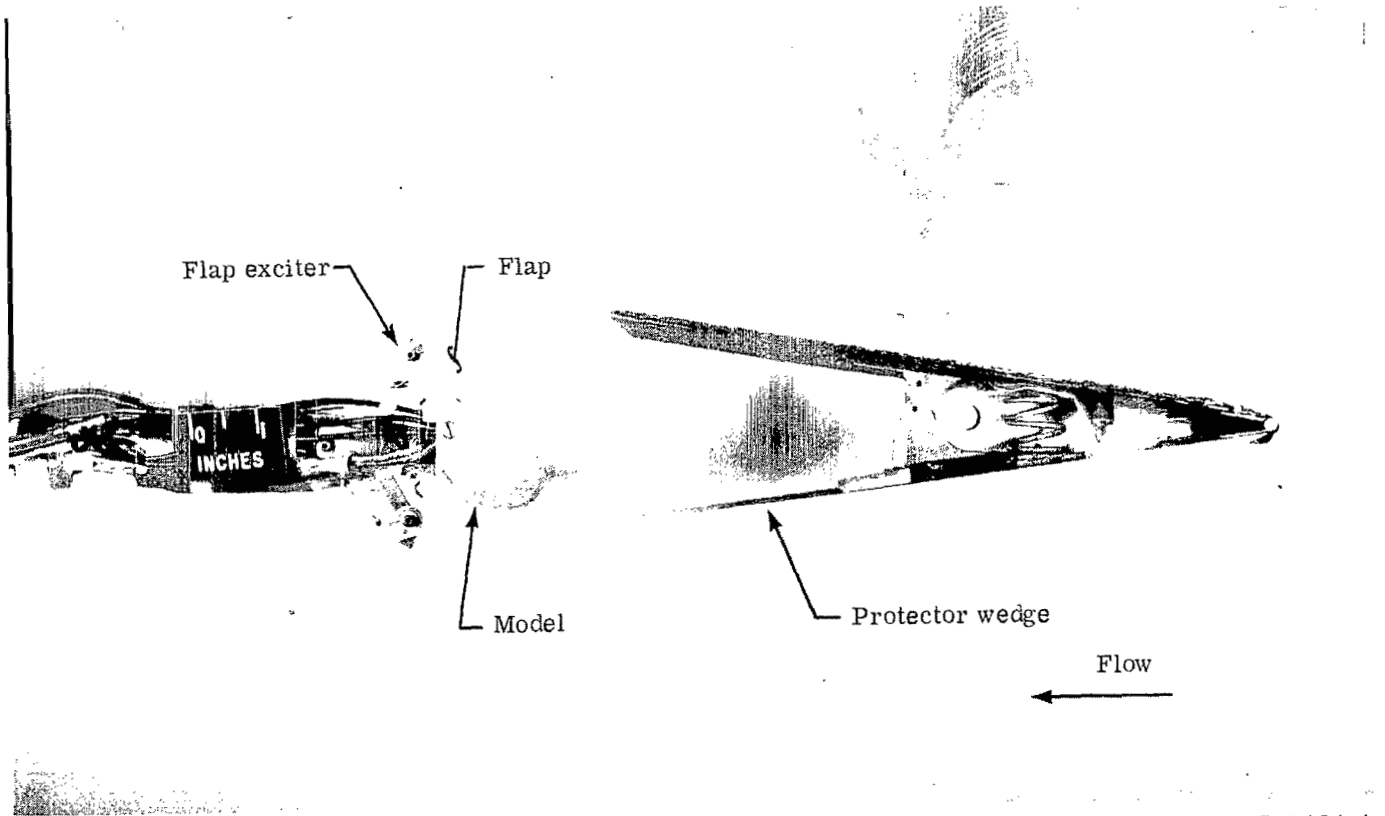

L-65-3131.1

(b) Model behind the protector wedge.

Figure 4.- Continued.

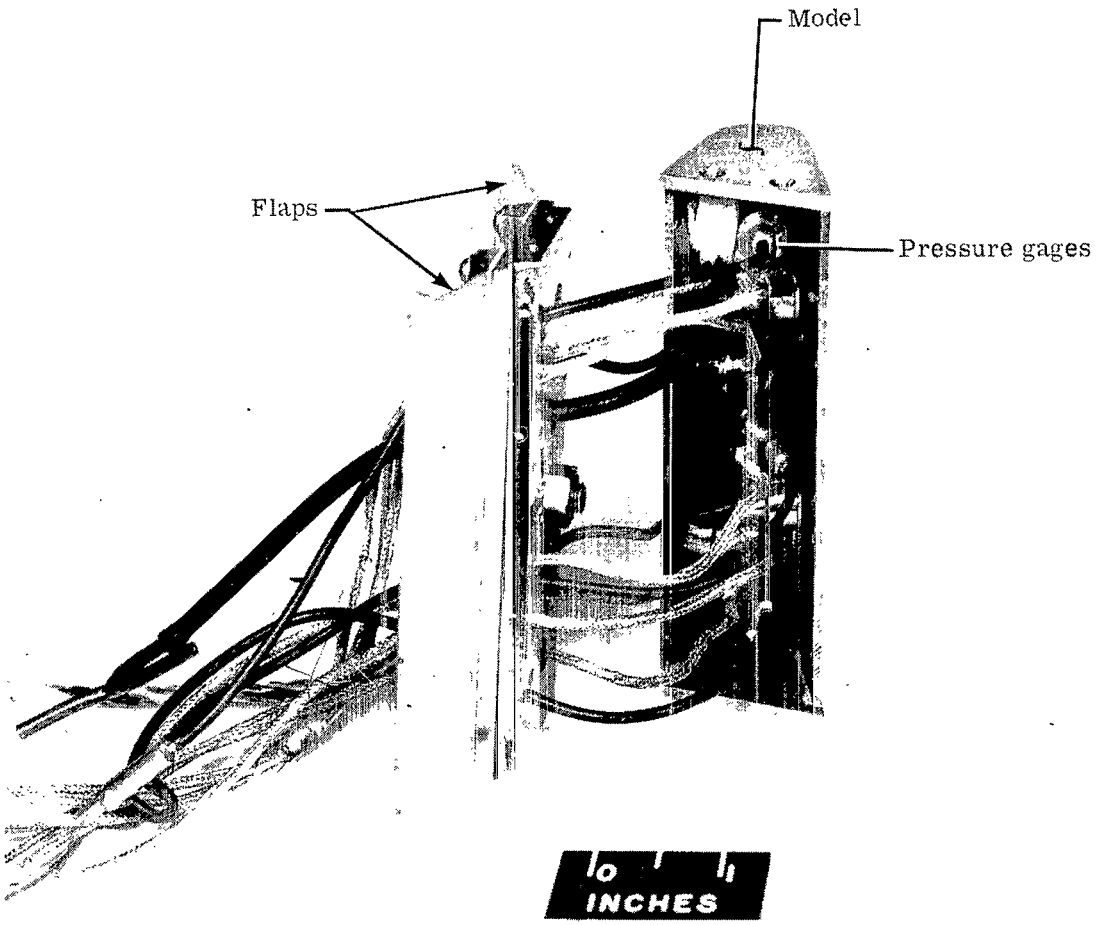

L-65-3135.1

(c) View of model showing installation of miniature pressure gages.

Figure 4.- Concluded.

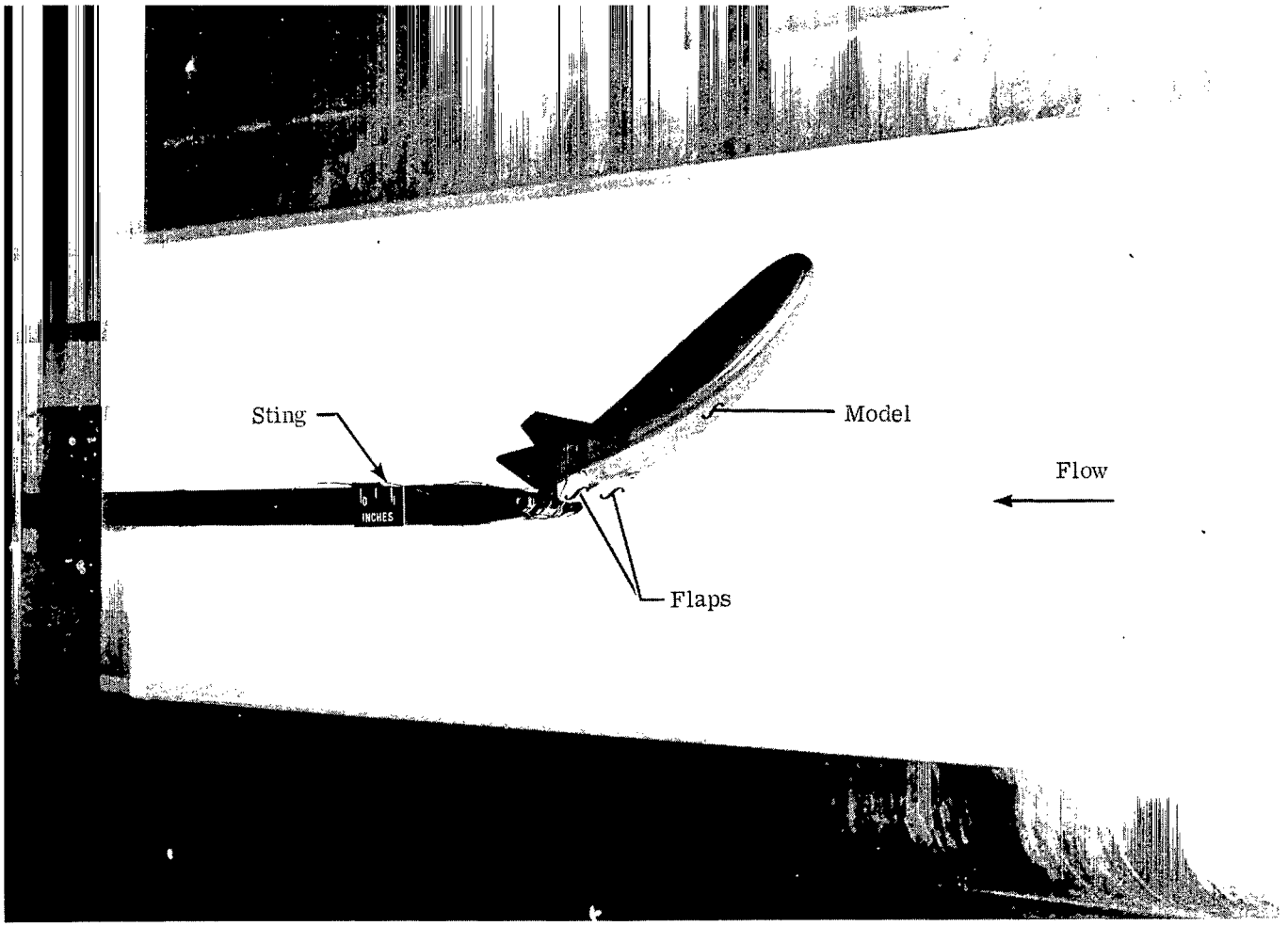

L-65-3124.1

(a) Model mounted on the sting.

Figure 5.- Photographs of three-dimensional model.

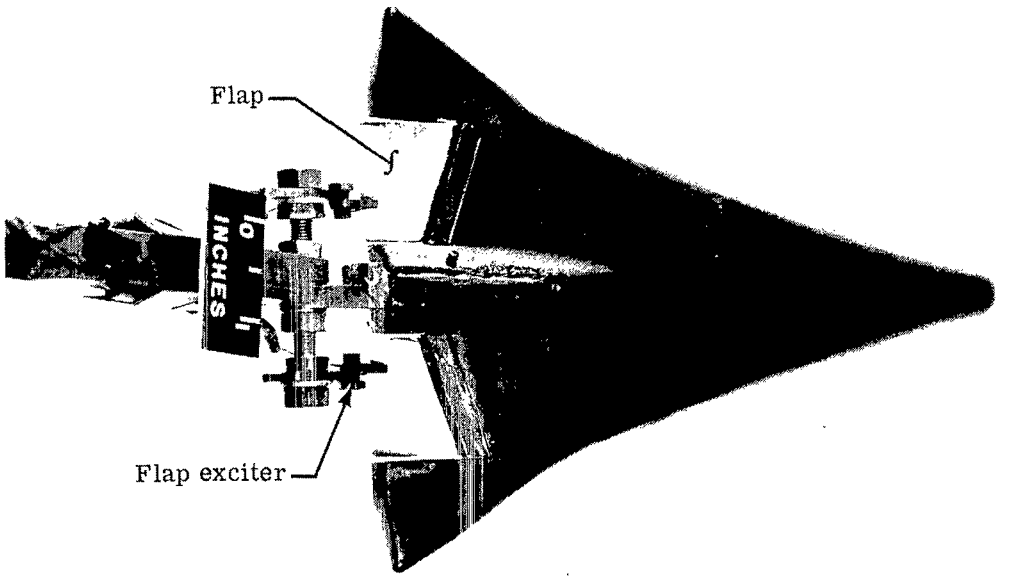

L-71-624

(b) Top view of model showing flaps and flap-exciter mechanism.

Figure 5.- Concluded.

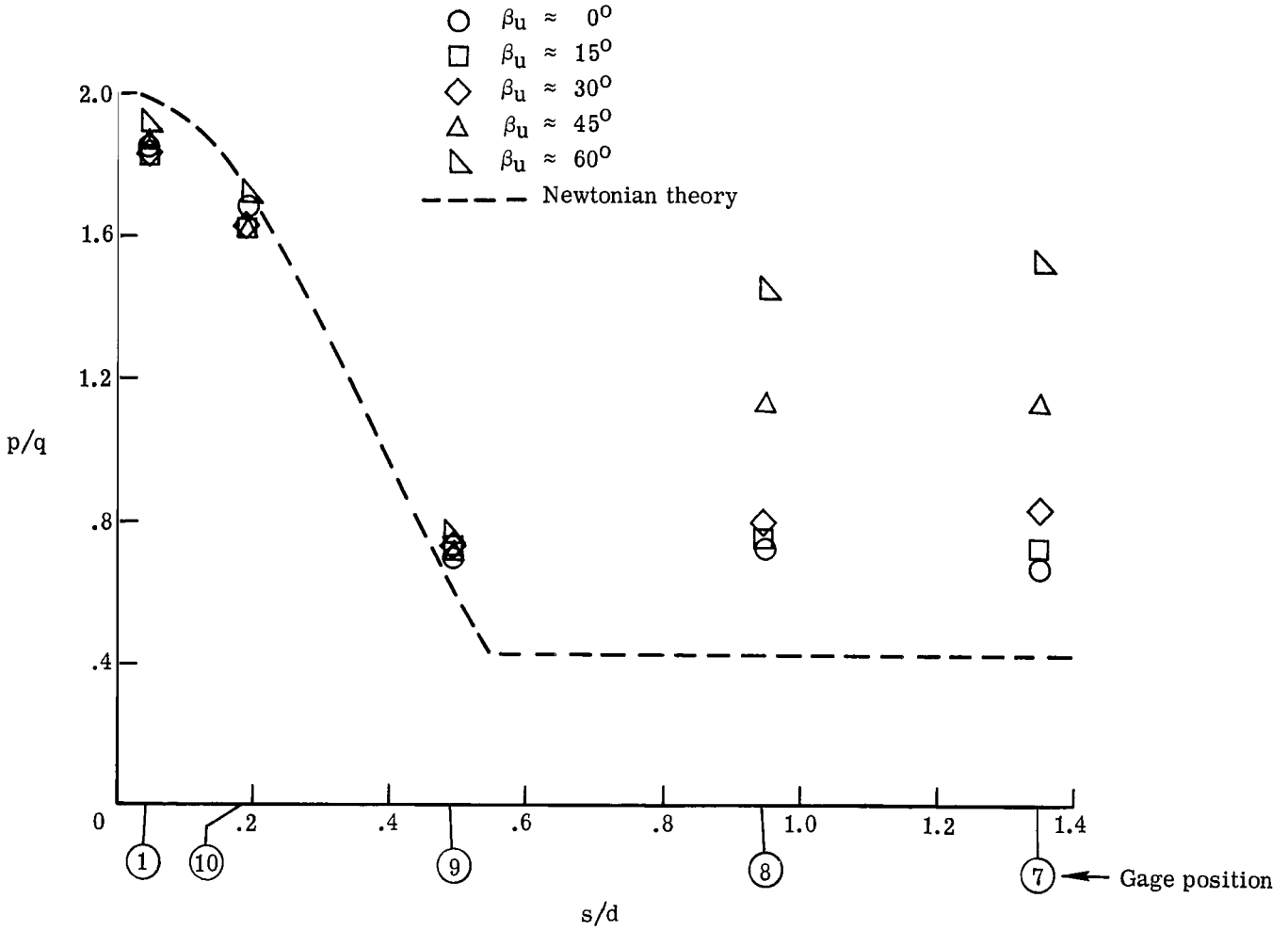

(a) Upper surface.

Figure 6.- Pressure distribution on two-dimensional configuration at $\alpha = 0^o$.

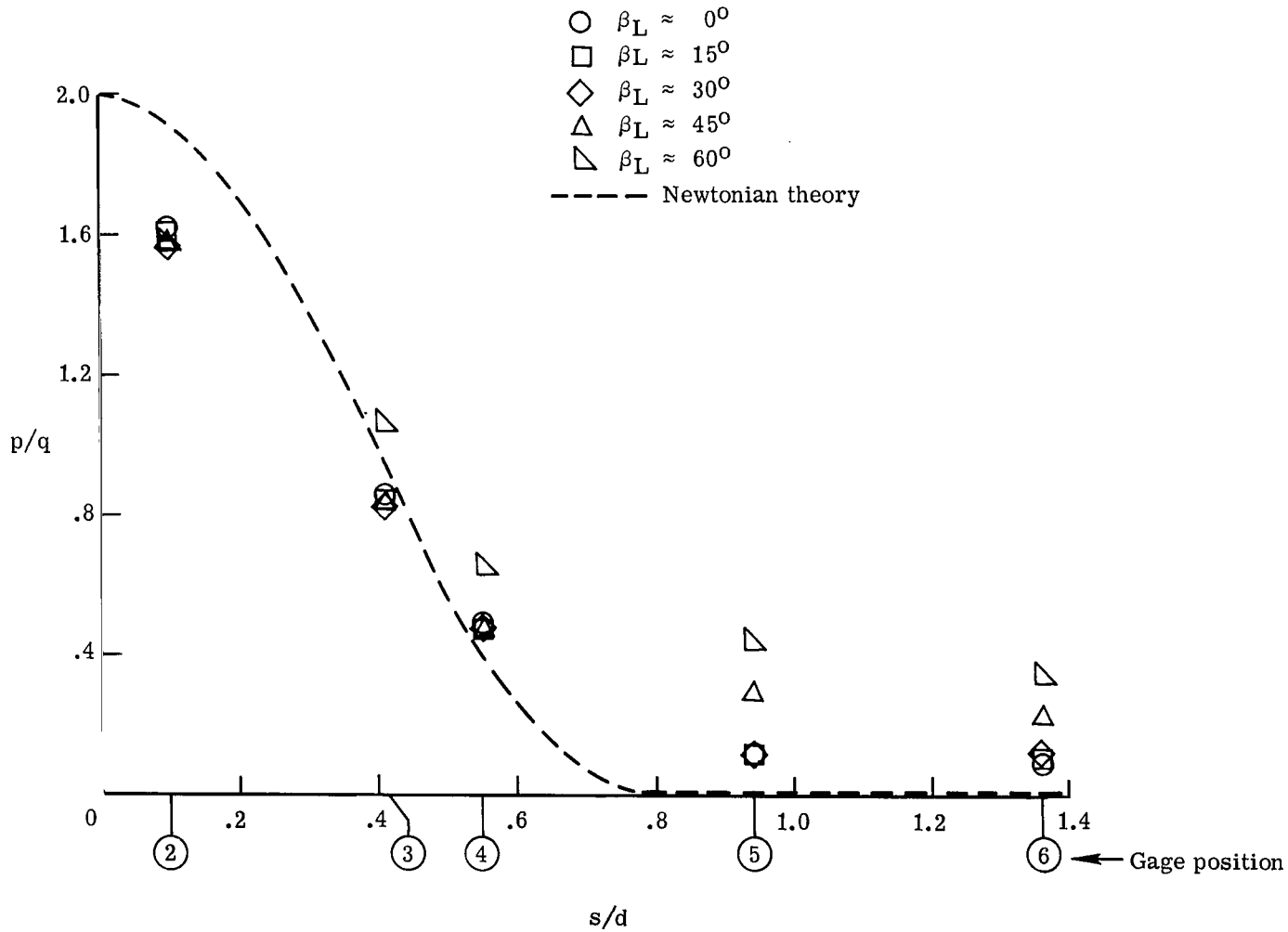

(b) Lower surface.

Figure 6.- Concluded.

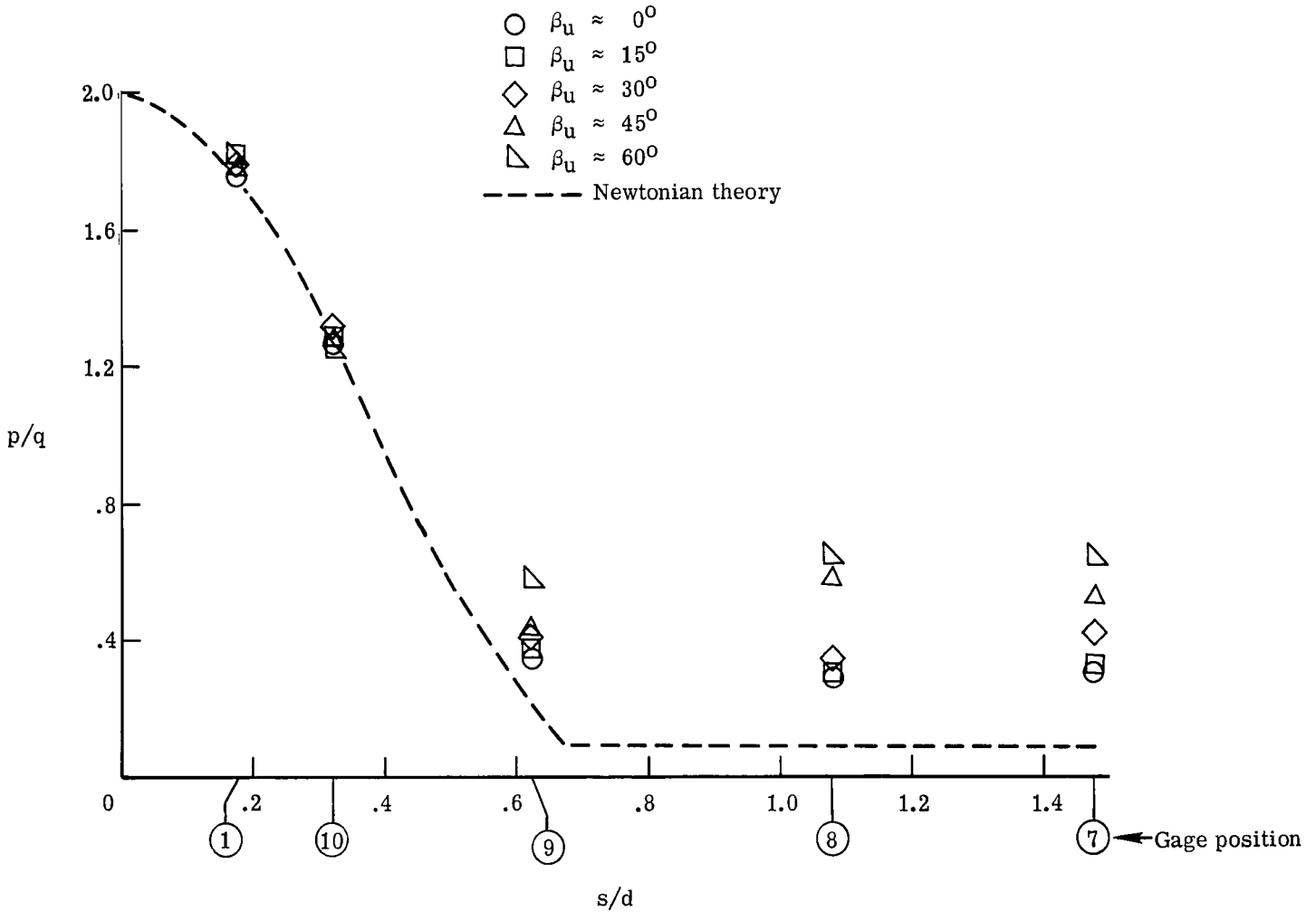

(a) Upper surface.

Figure 7.- Pressure distribution on two-dimensional configuration at $\alpha = 15^o$.

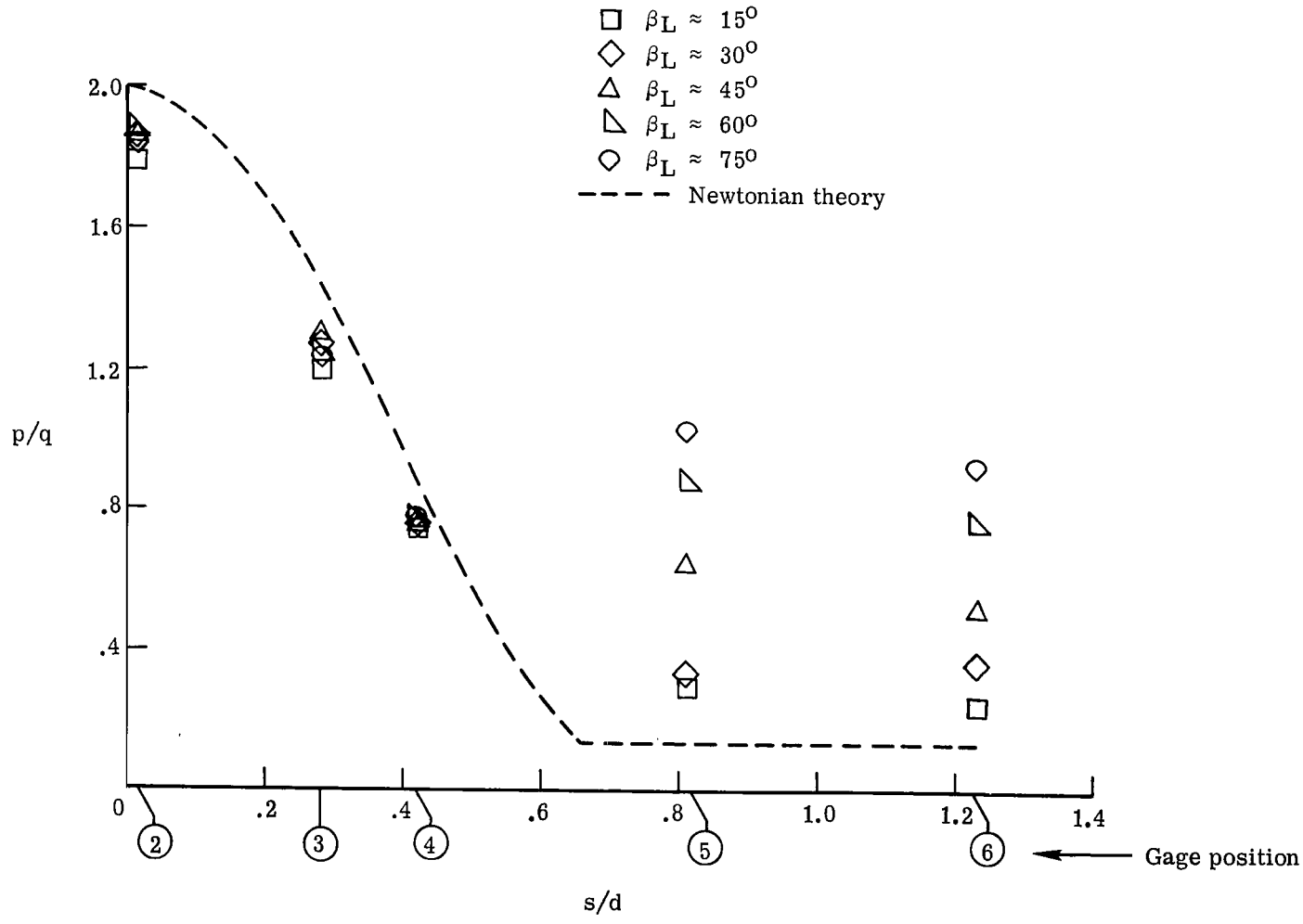

(b) Lower surface.

Figure 7.- Concluded.

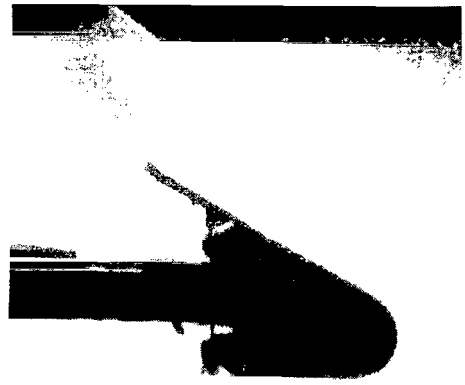

(a) Run 6. $\alpha = 0^{o}$; $\beta_L = 0^{o}$; $\beta_u = 0^{o}$.

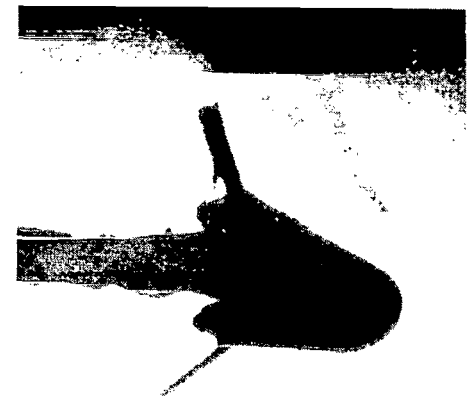

(b) Run 4. $\alpha = 0^{o}$; $\beta_L = 43^{o}$; $\beta_u = 41^{o}$.

(c) Run 8. $\alpha = 15^{o}$; $\beta_L = 16^{o}$; $\beta_u = 1^{o}$.

L-71-625

(d) Run 23. $\alpha = 15^{o}$; $\beta_L = 29^{o}$; $\beta_u = 14^{o}$.

Figure 8.- Schlieren photographs depicting the flow field of the two-dimensional configuration.

(e) Run 22. $\alpha = 15^{o}$; $\beta_L = 45^{o}$; $\beta_u = 30^{o}$.

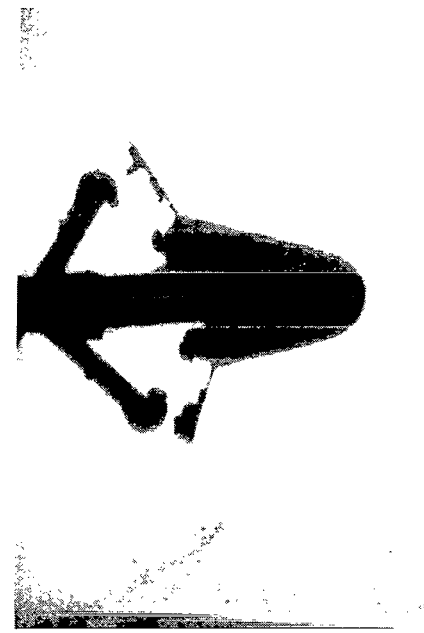

(f) Run 15. $\alpha = 15^{o}$; $\beta_L = 61^{o}$; $\beta_u = 44^{o}$.

L-71-626

(g) Run 17. $\alpha = 15^{o}$; $\beta_L = 73^{o}$; $\beta_u = 57^{o}$.

Figure 8.- Concluded.

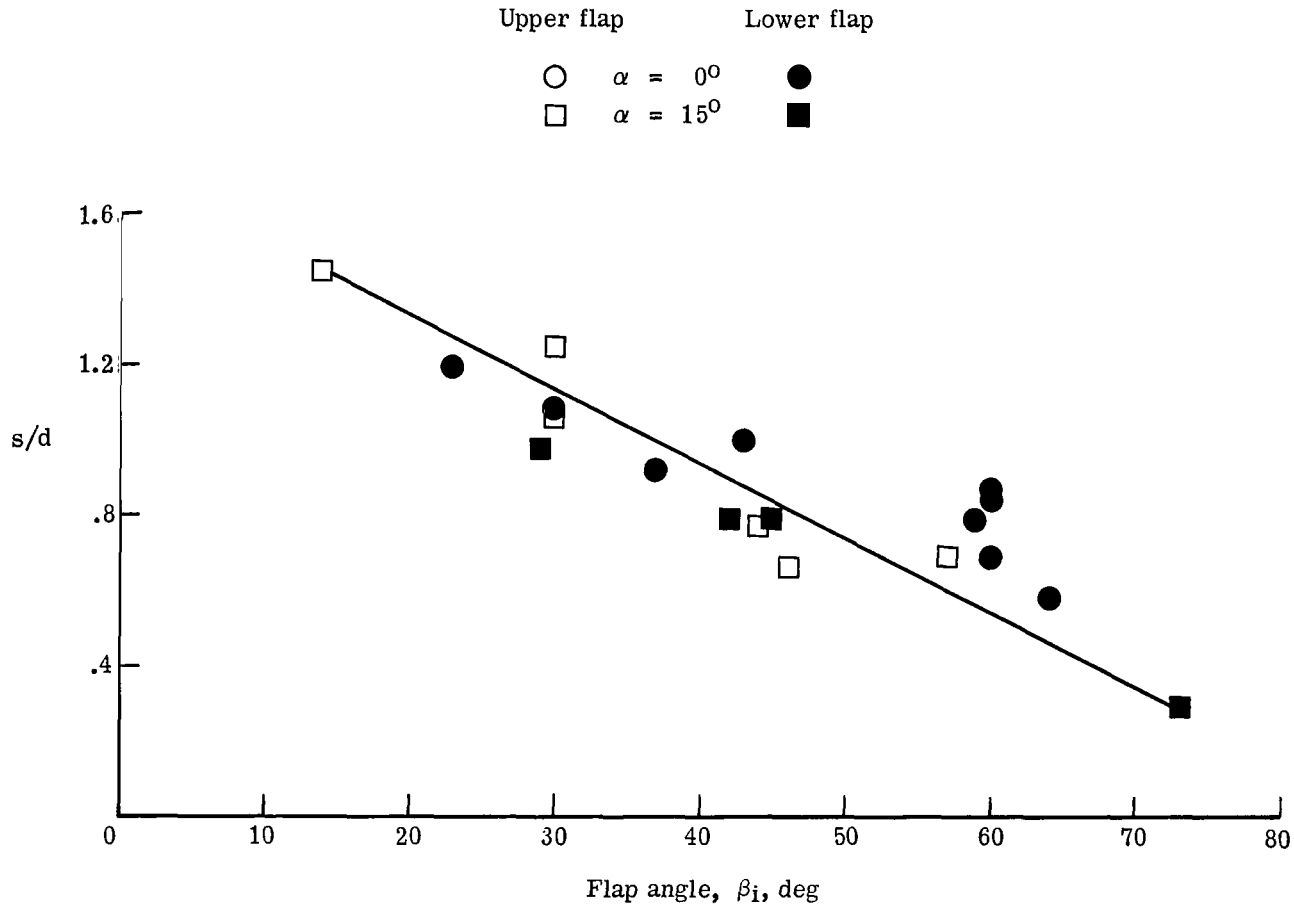

Figure 9.- Variation of separation-point location with control flap angle on two-dimensional configuration.

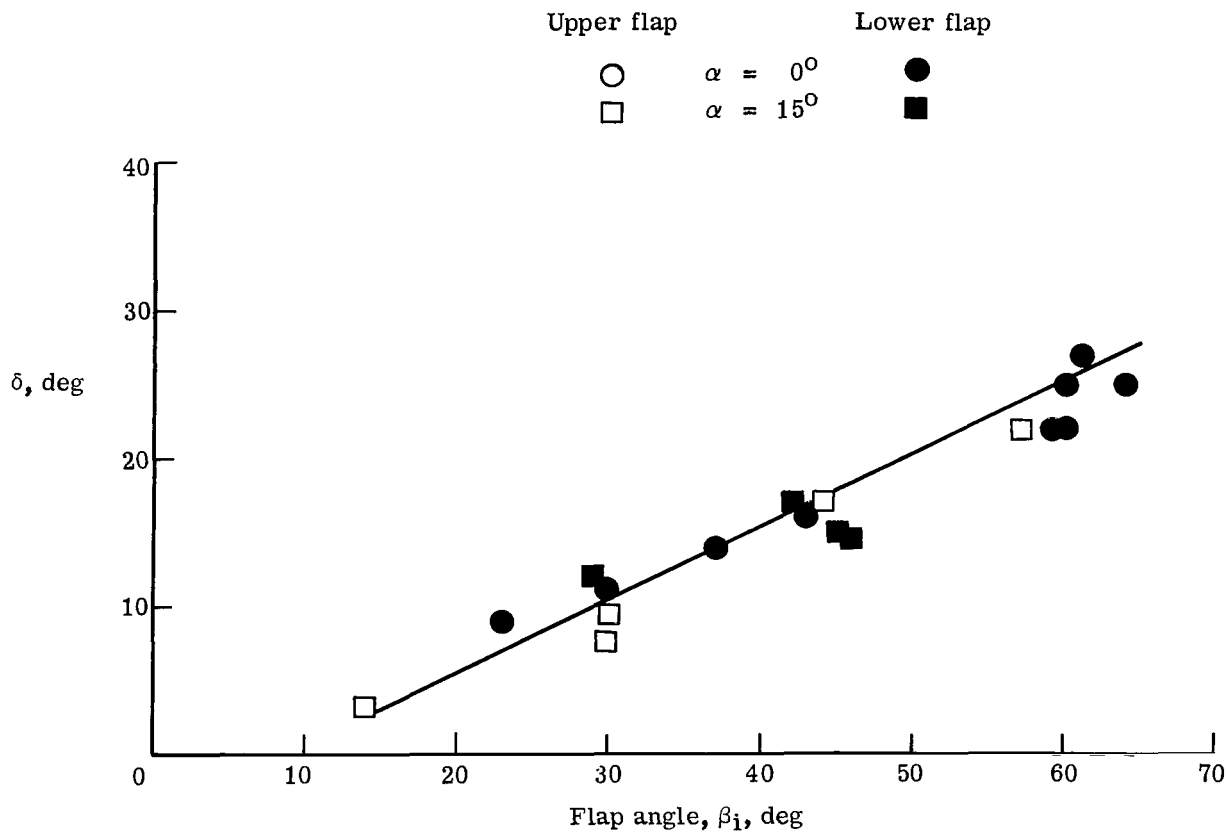

Figure 10.- Variation of local separation-wedge angle δ with control flap angle on two-dimensional configuration.

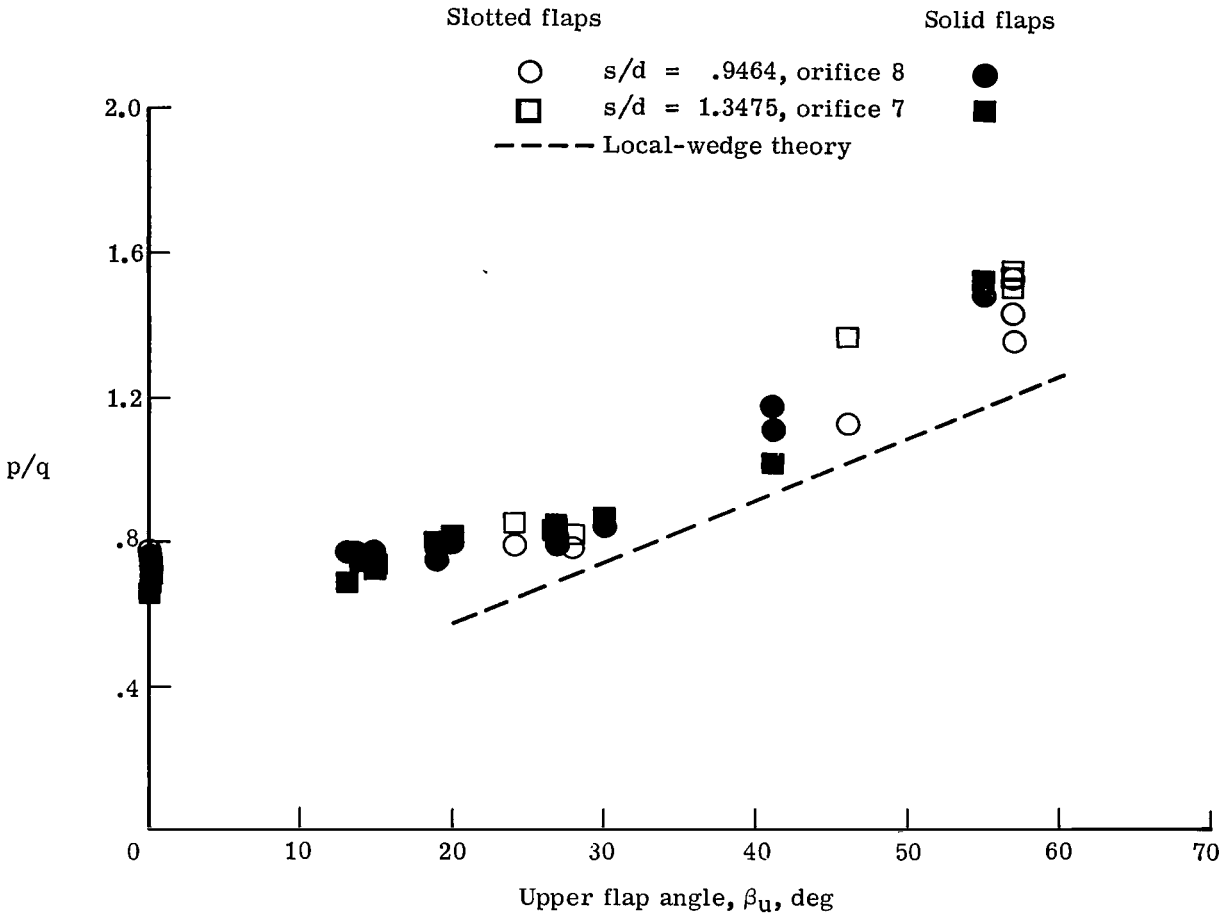

(a) Upper surface.

Figure 11.- Pressure measurements ahead of control flaps as a function of flap angle for two-dimensional configuration at $\alpha = 0^{o}$.

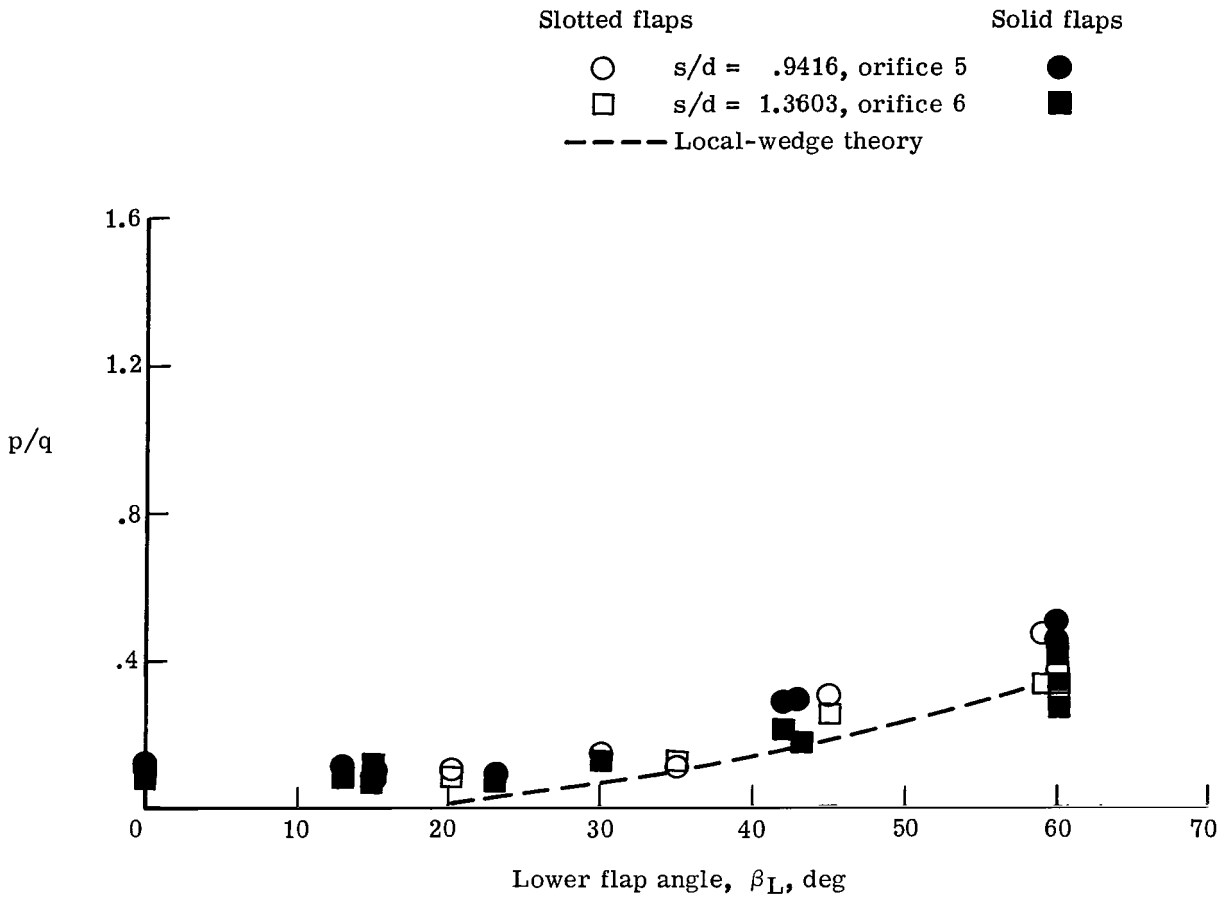

(b) Lower surface.

Figure 11.- Concluded.

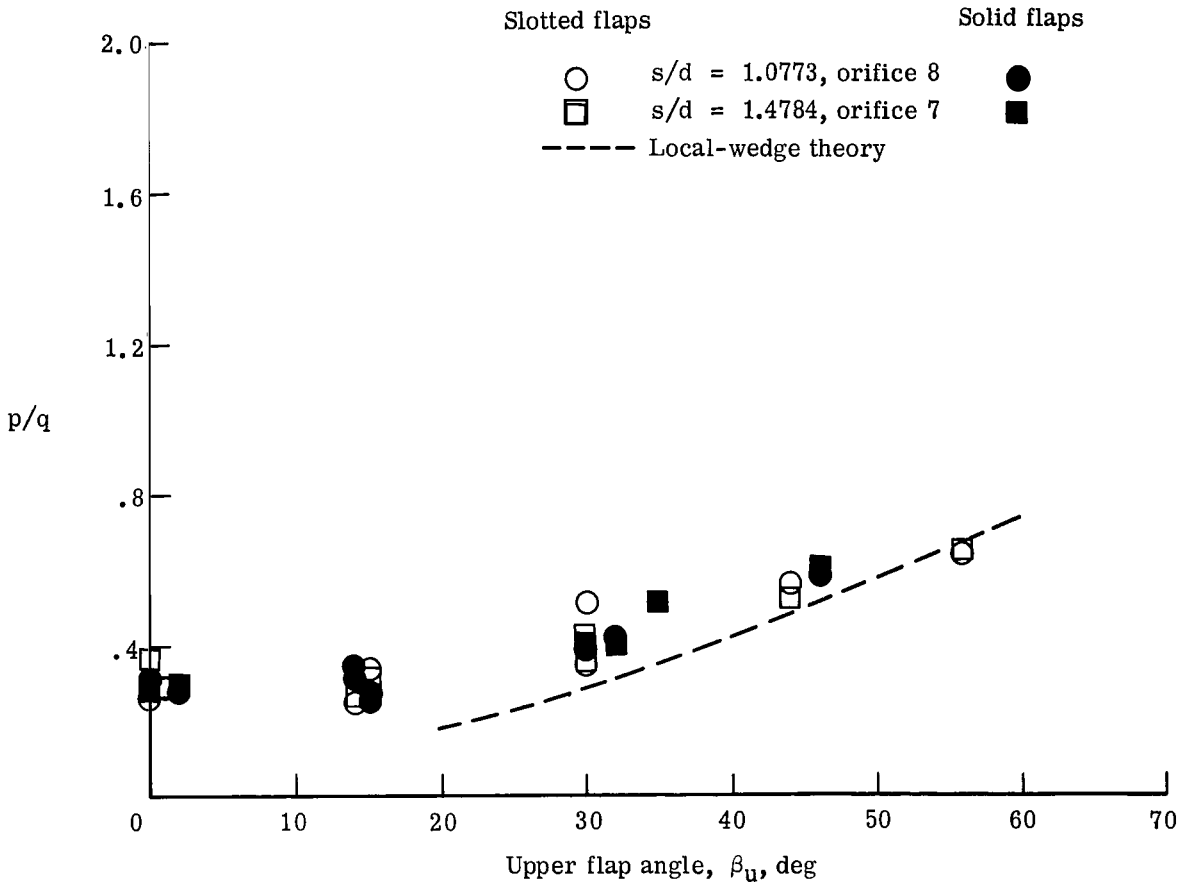

(a) Upper surface.

Figure 12.- Pressure measurements ahead of control flaps as a function of flap angle for two-dimensional configuration at $\alpha = 15^{o}$.

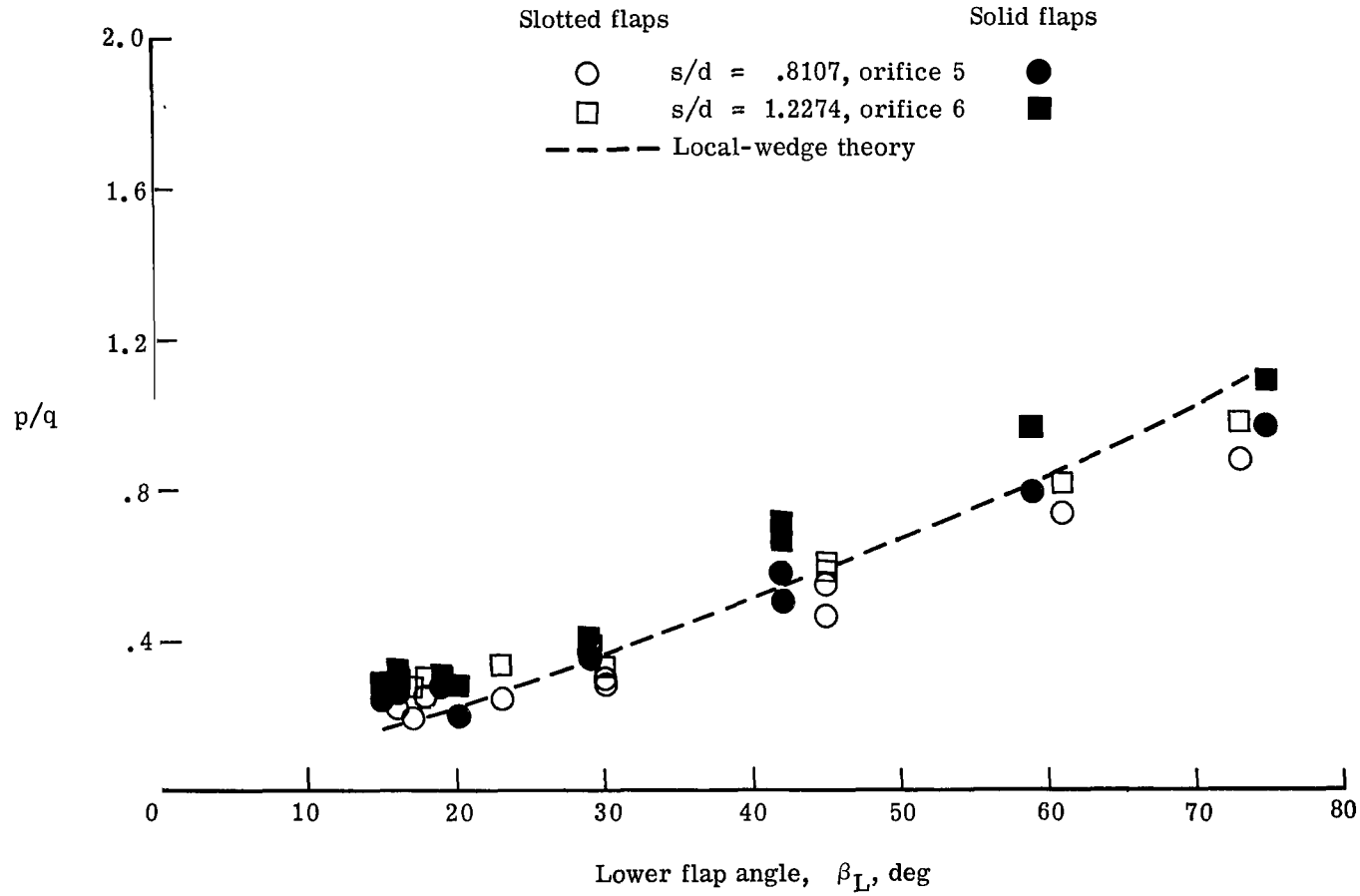

(b) Lower surface.

Figure 12.- Concluded.

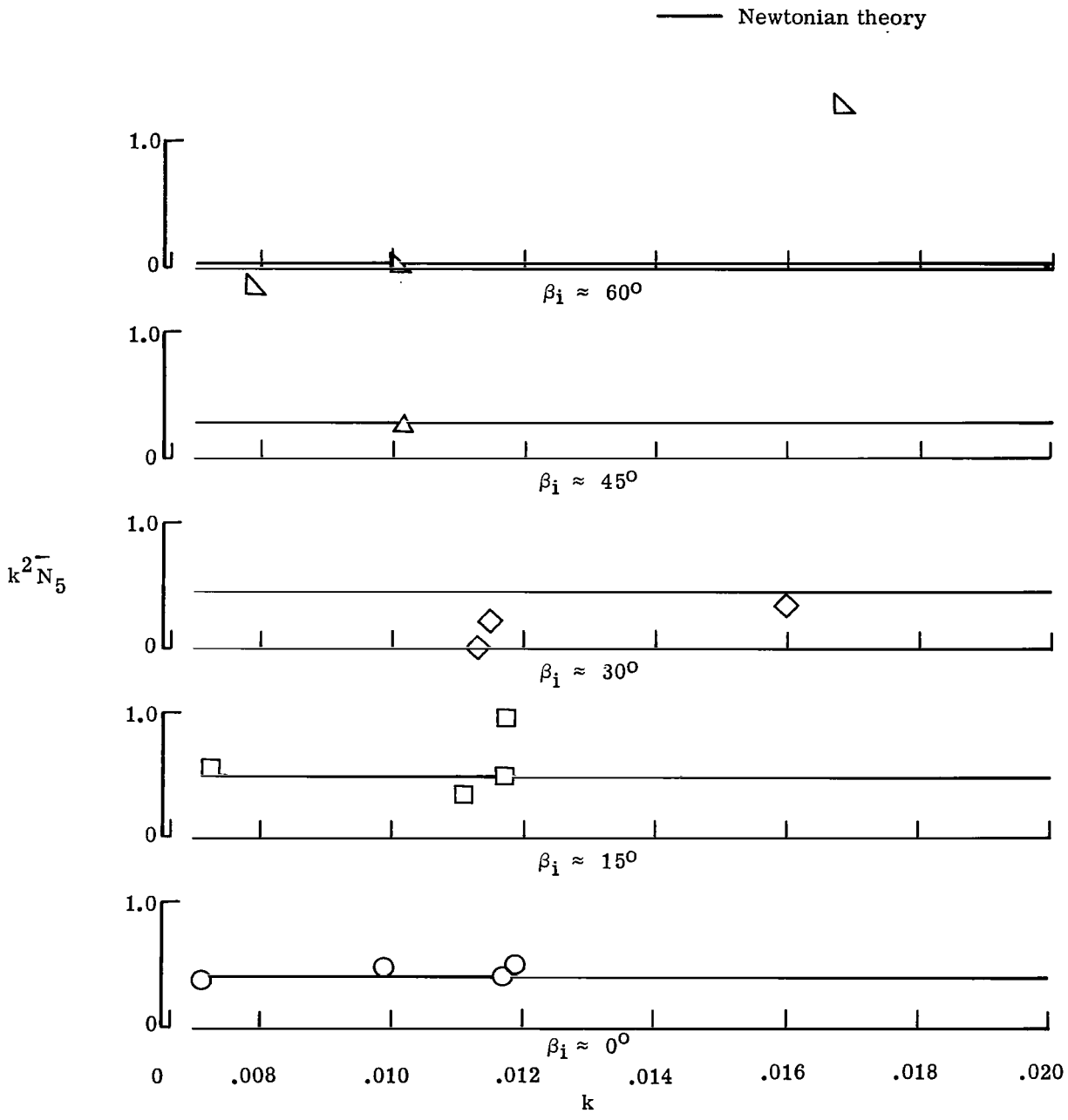

(a) Upper surface.

Figure 13.- Variation of the aerodynamic stiffness parameter with reduced frequency for the two-dimensional model at $\alpha = 0^o$.

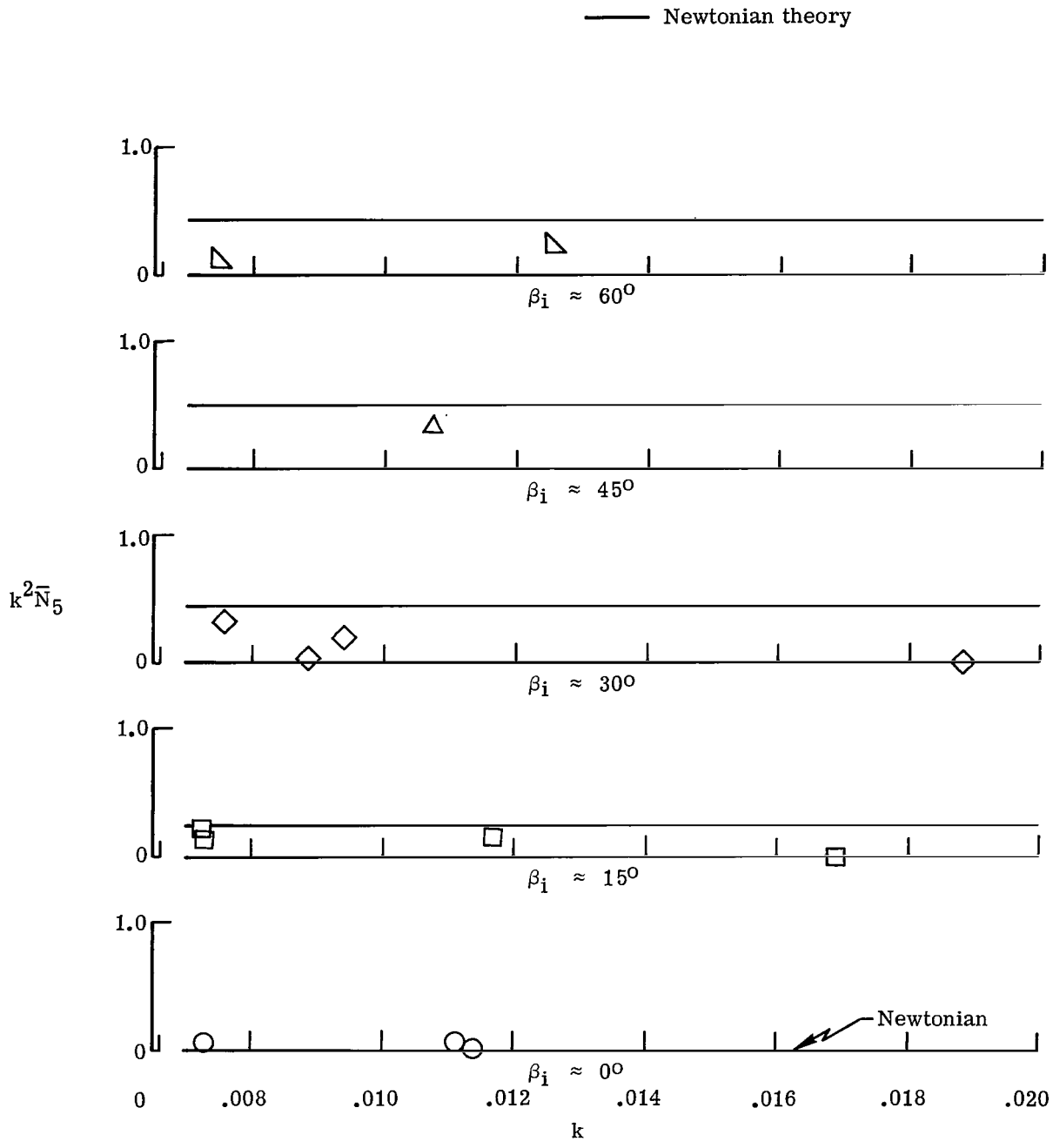

(b) Lower surface.

Figure 13.- Concluded.

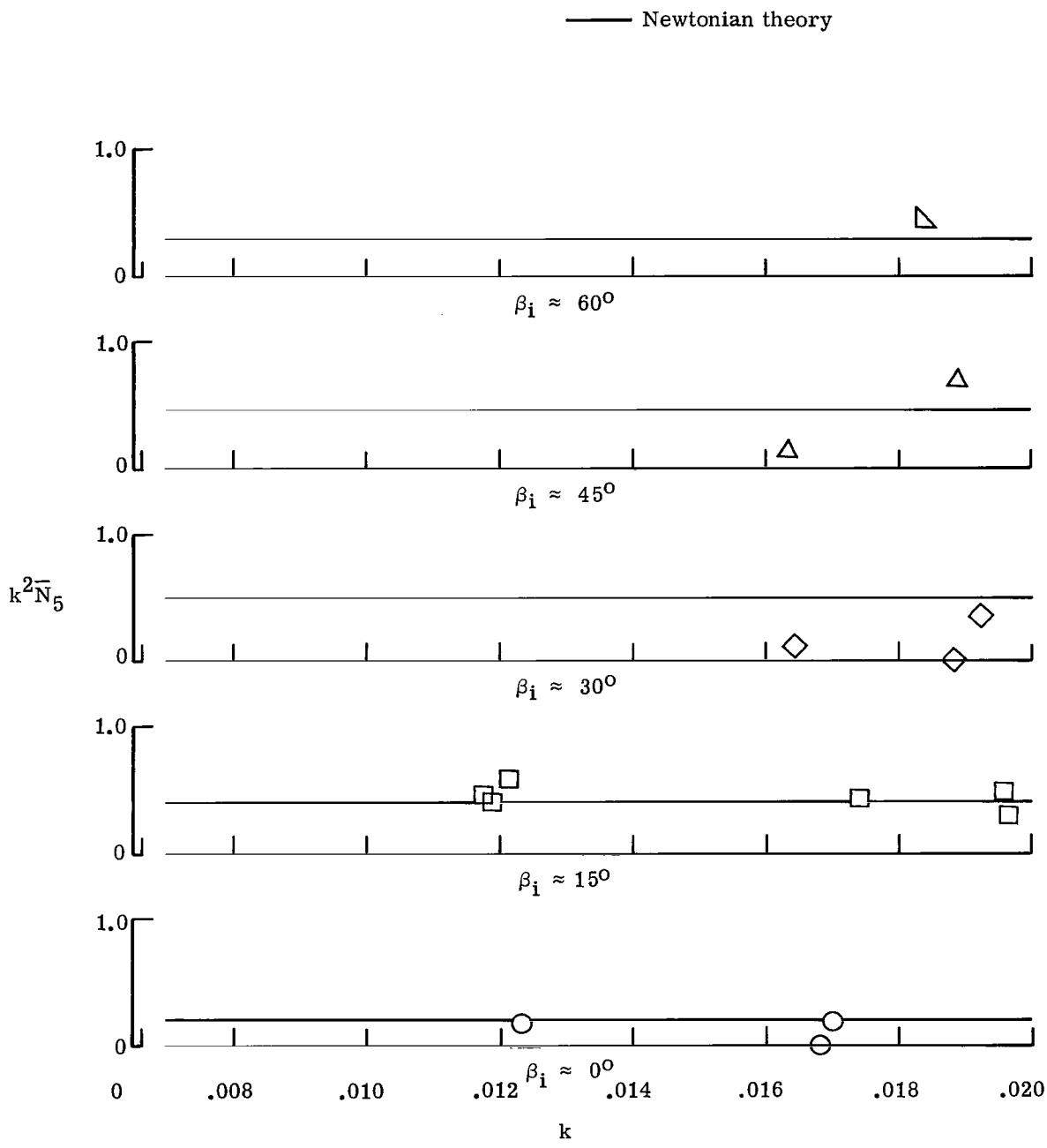

(a) Upper surface.

Figure 14.- Variation of the aerodynamic stiffness parameter with reduced frequency for the two-dimensional model at $\alpha = 15^o$.

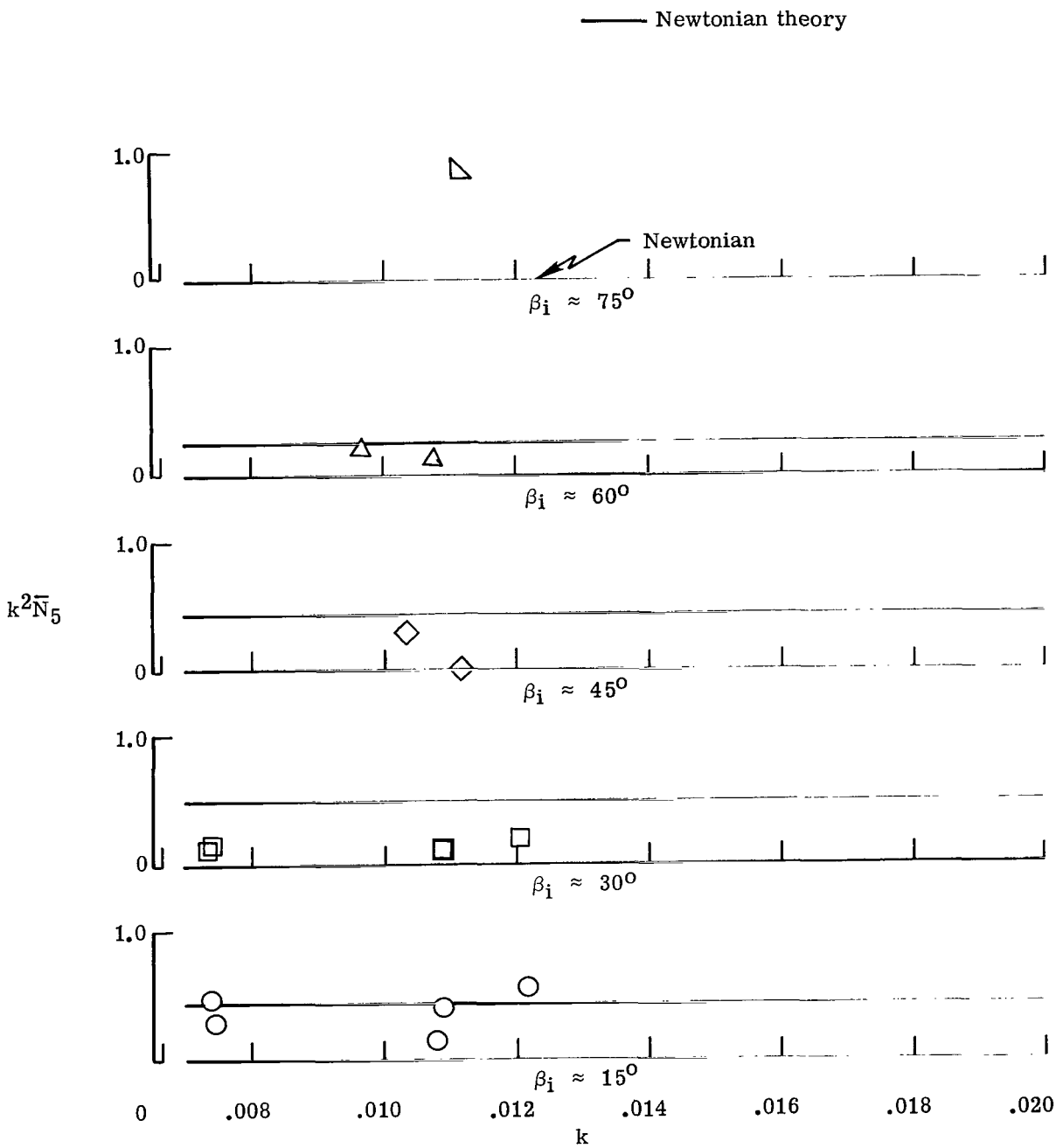

(b) Lower surface.

Figure 14.- Concluded.

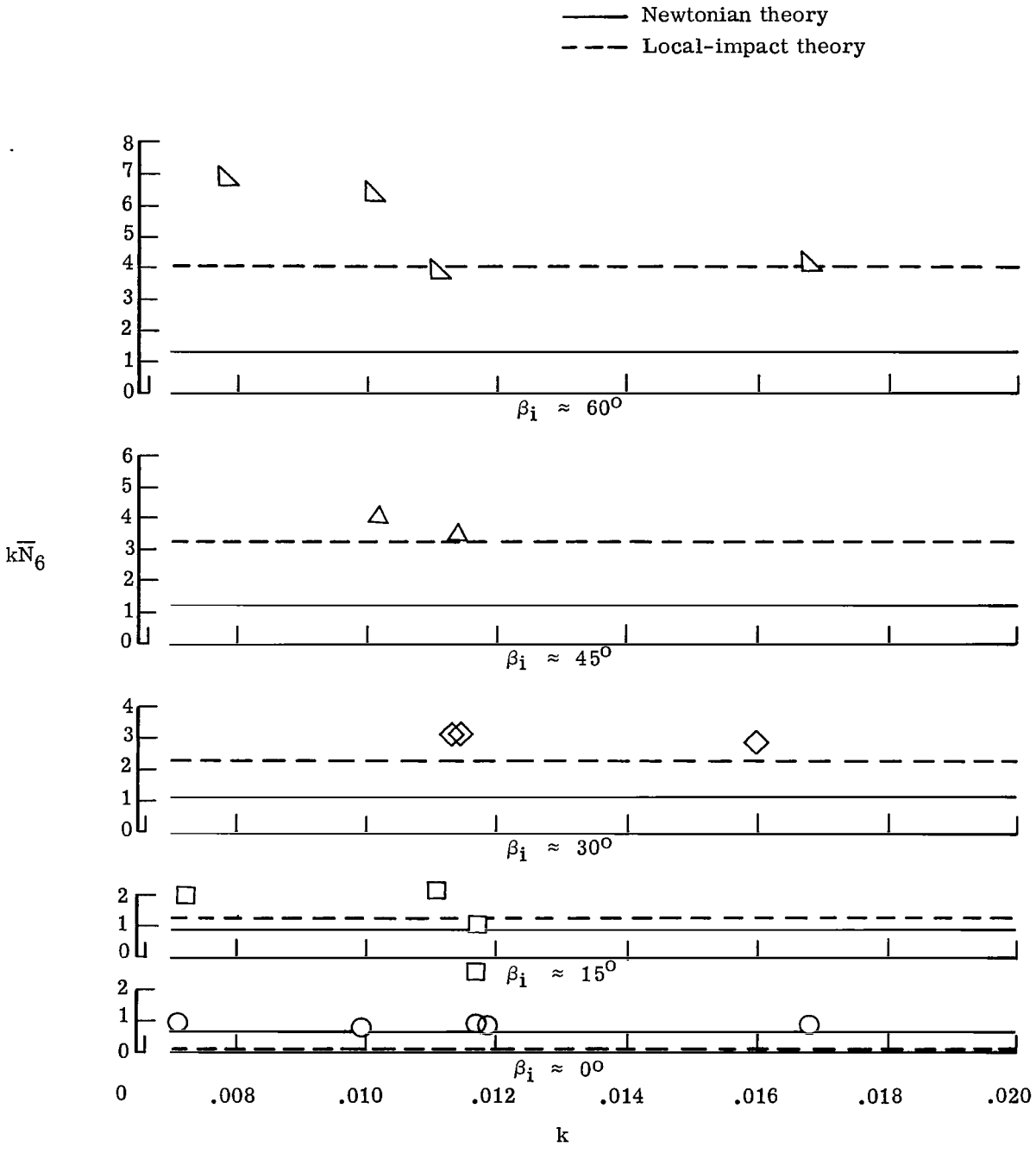

(a) Upper flap.

Figure 15.- Variation of the aerodynamic damping parameter with reduced frequency for the two-dimensional model at $\alpha = 0^o$.

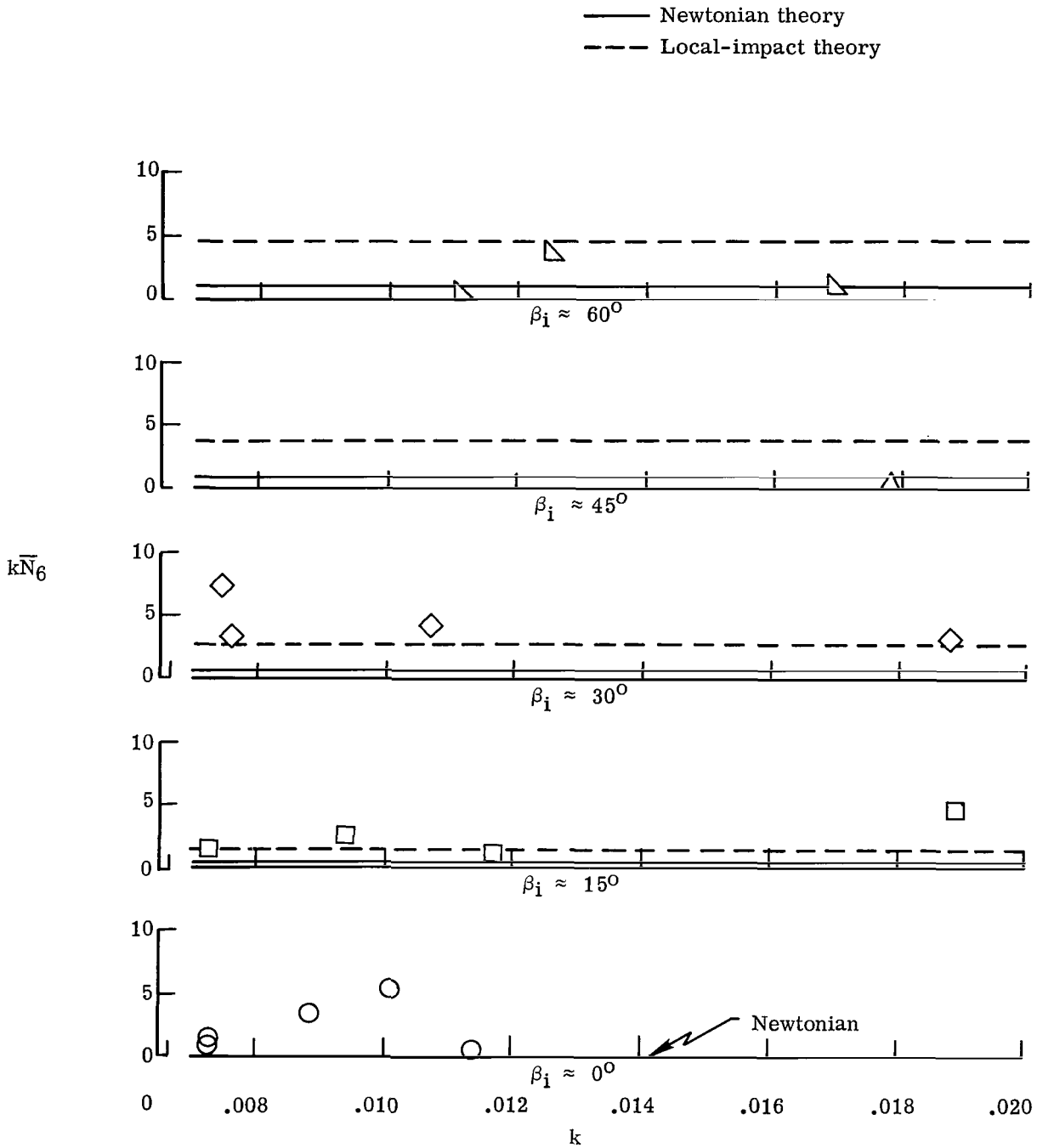

(b) Lower flap.

Figure 15.- Concluded.

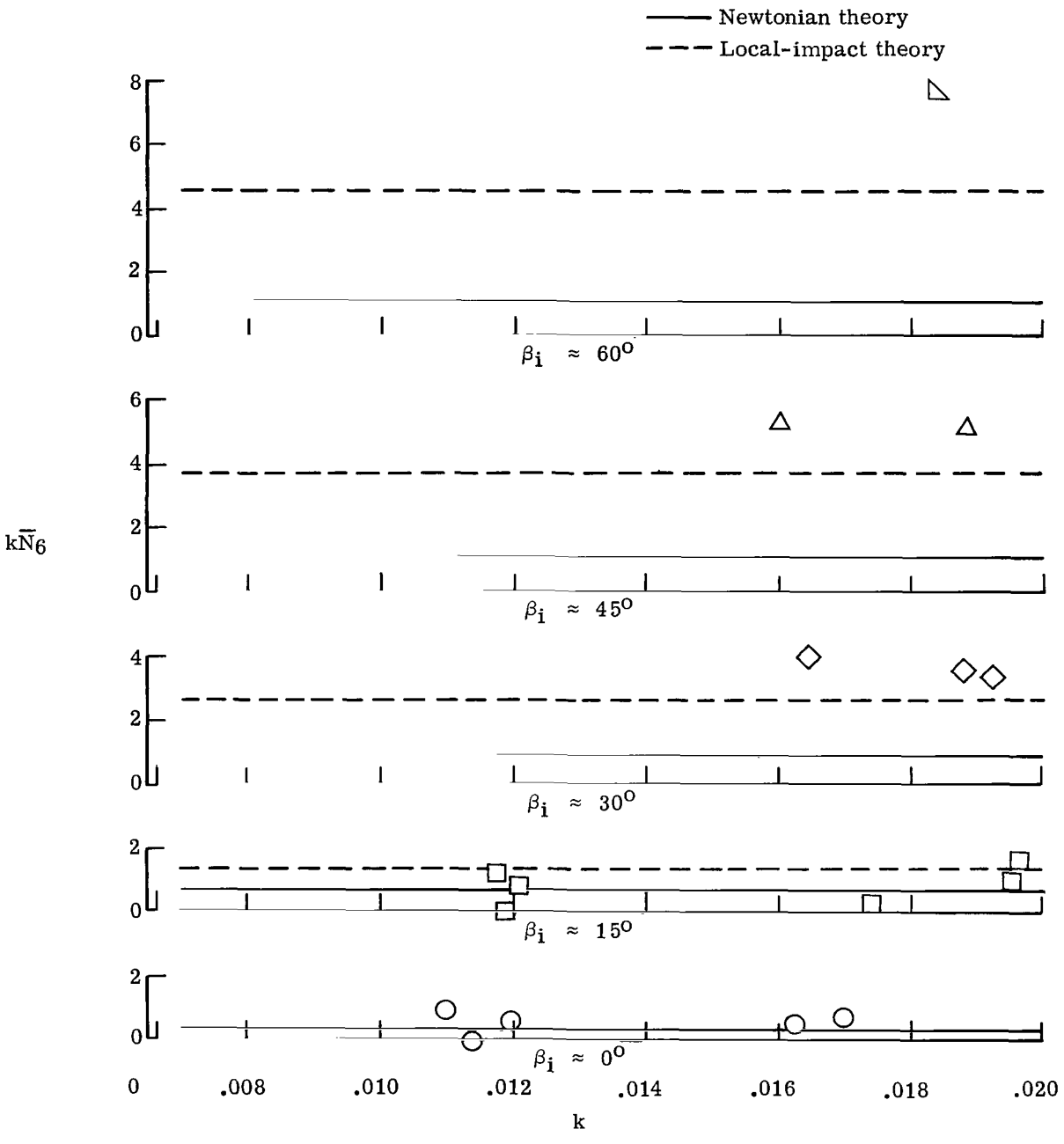

(a) Upper flap.

Figure 16.- Variation of the aerodynamic damping parameter with reduced frequency for the two-dimensional model at $\alpha = 15^o$.

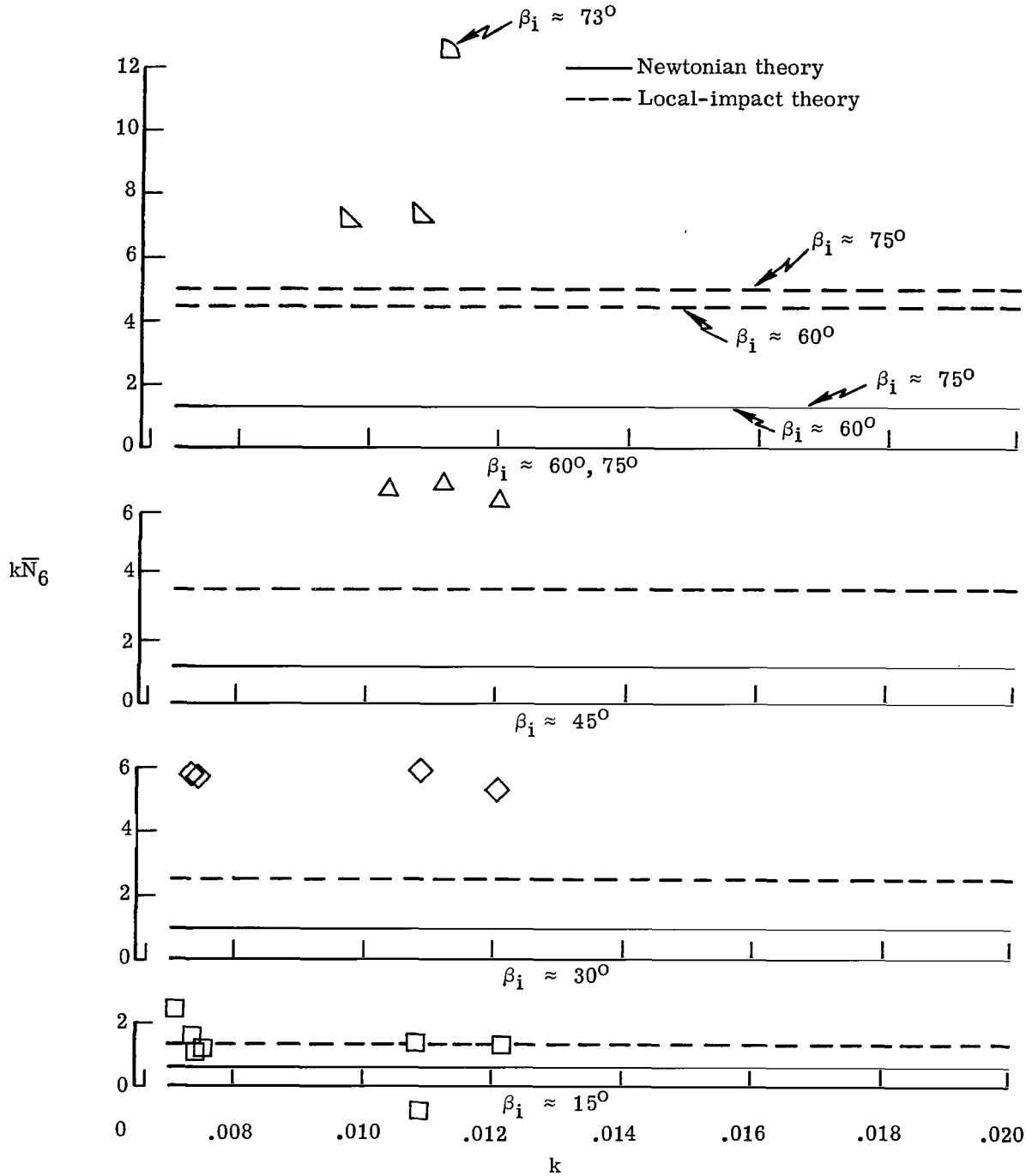

(b) Lower flap.

Figure 16.- Concluded.

(a) Run 39. $\alpha = 0^{o}$; $\beta_s = 36.5^{o}$; $\beta_p = 40.5^{o}$.

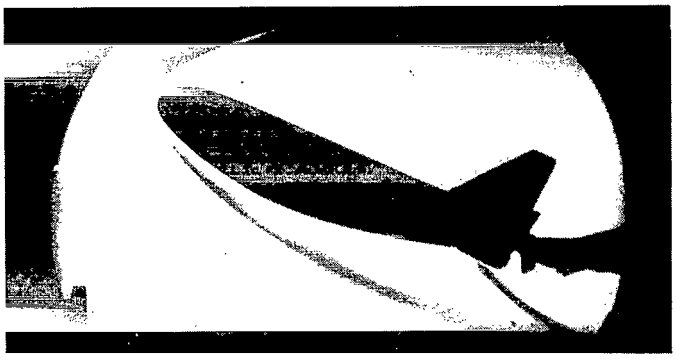

(b) Run 37. $\alpha = 25^{o}$; $\beta_s = 17^{o}$; $\beta_p = 19^{o}$.

L-71-627

(c) Run 47. $\alpha = 25^{o}$; $\beta_s = 50^{o}$; $\beta_p = 58^{o}$.

Figure 17.- Schlieren photographs depicting the flow field of the three-dimensional configuration.

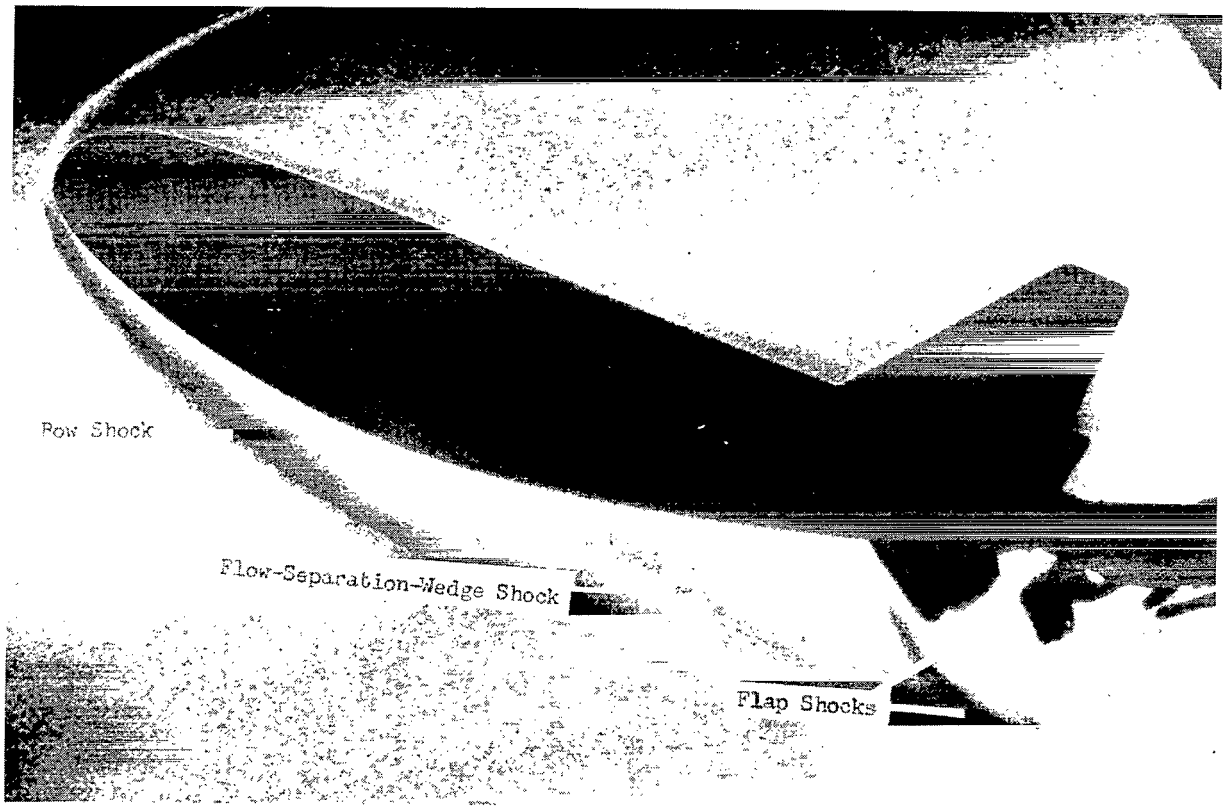

L-71-628

(d) Run 40. $\alpha = 25^{o}$; $\beta_s = 40^{o}$; $\beta_p = 36^{o}$.

Figure 17.- Concluded.

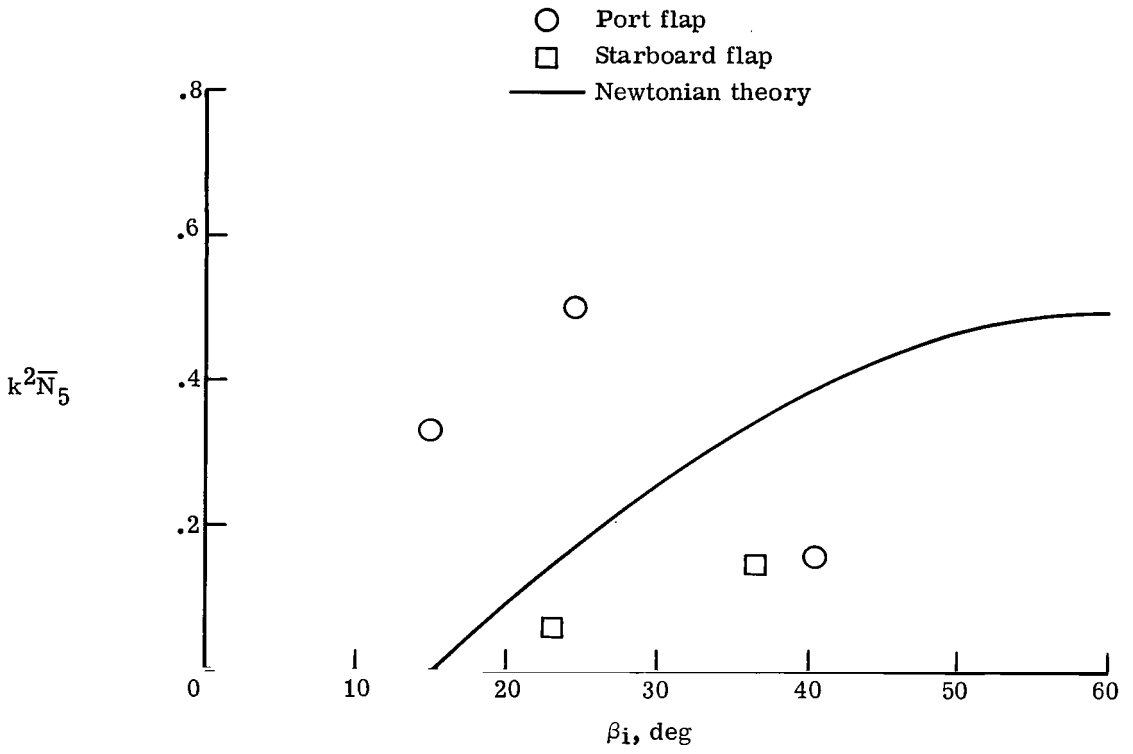

(a) $\alpha = 0^o$.

Figure 18.- Variation of aerodynamic stiffness parameter with flap angle for three-dimensional configuration.

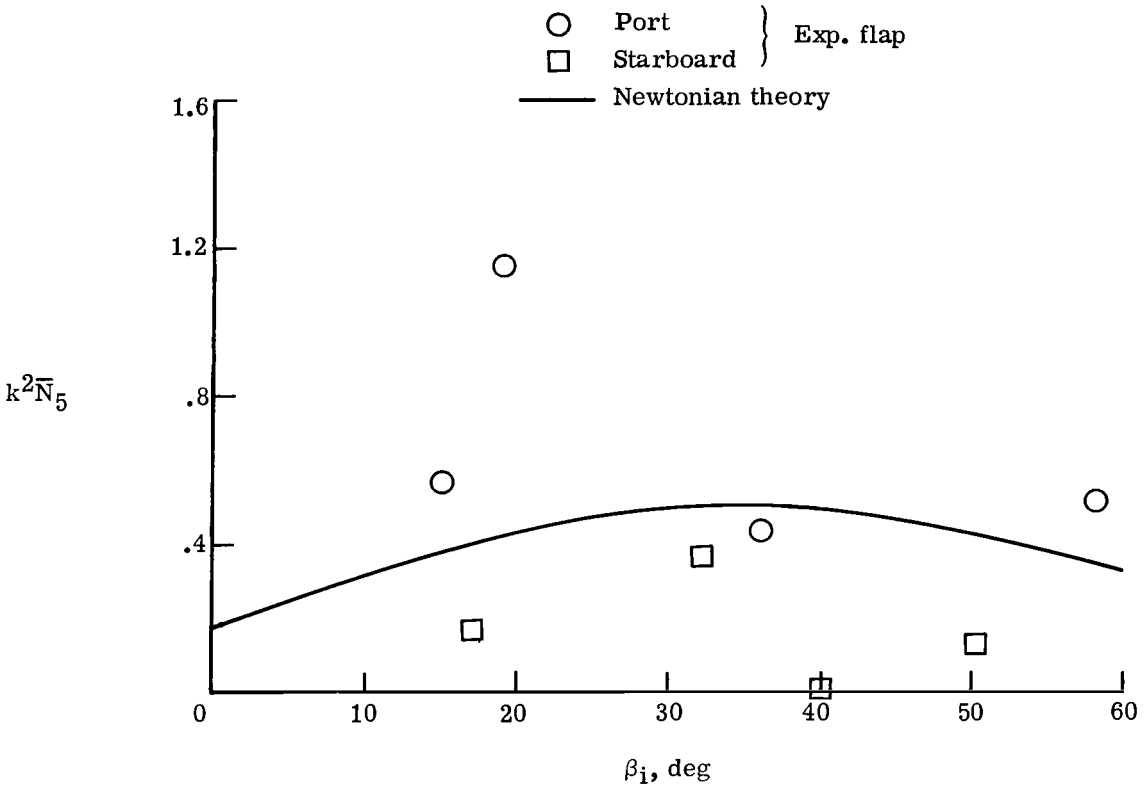

(b) $\alpha = 25^{\circ}$.

Figure 18.- Concluded.

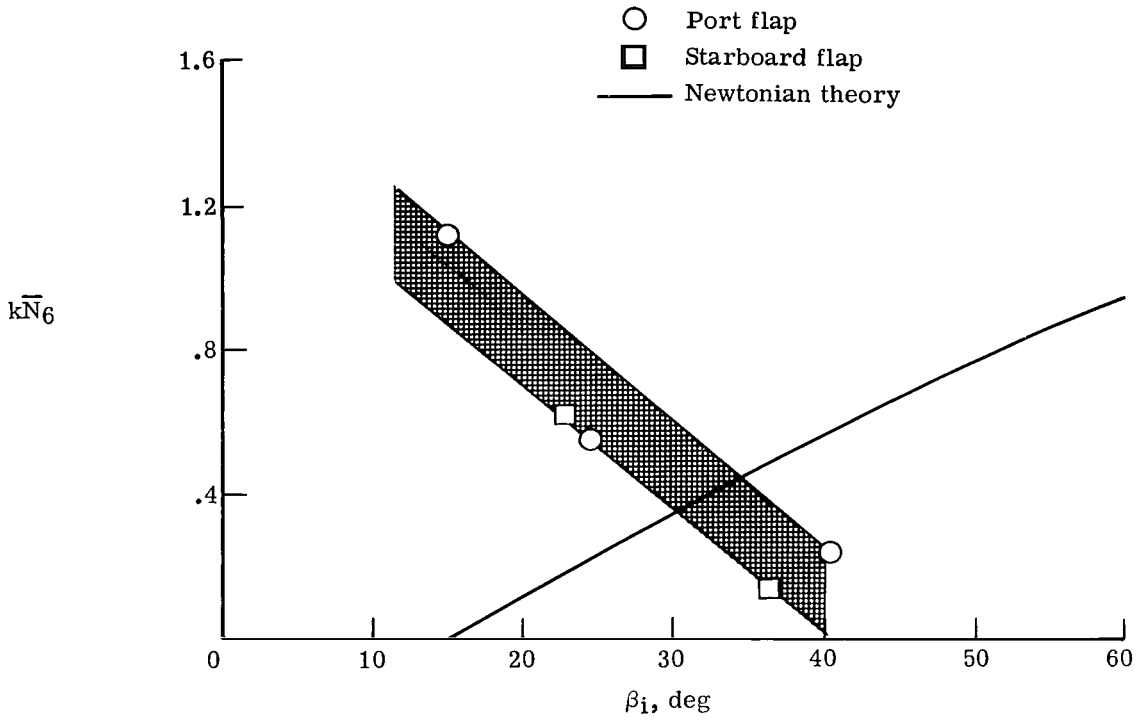

(a) $\alpha = 0^o$.

Figure 19.- Variation of aerodynamic damping parameter with flap angle for the three-dimensional configuration. Band illustrates decreasing trend of aerodynamic damping with increasing flap angle at both angles of attack.

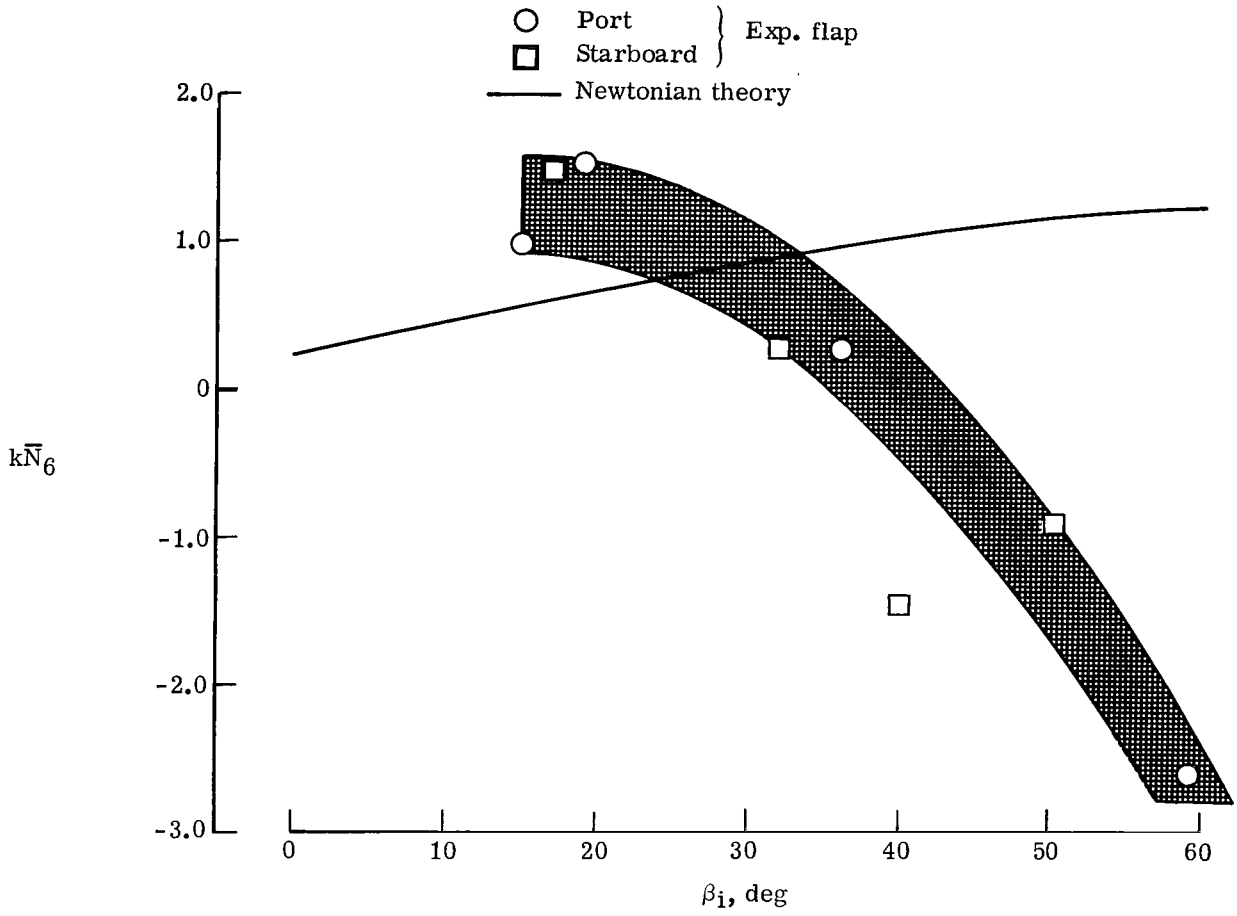

(b) $\alpha = 25^{\circ}$.

Figure 19.- Concluded.

NASA-Langley, 1971 —— 31 L-7610

NATIONAL AERONAUTICS AND SPACE ADMINISTRATION
WASHINGTON, D. C. 20546

OFFICIAL BUSINESS
PENALTY FOR PRIVATE USE $300

FIRST CLASS MAIL

POSTAGE AND FEES PAID
NATIONAL AERONAUTICS AND
SPACE ADMINISTRATION

002 001 C1 U 31 710730 S00903DS
DEPT OF THE AIR FORCE
WEAPONS LABORATORY /WLOL/
ATTN: E LOU BOWMAN, CHIEF TECH LIBRARY
KIRTLAND AFB NM 87117

POSTMASTER: If Undeliverable (Section 158 Postal Manual) Do Not Return

"The aeronautical and space activities of the United States shall be conducted so as to contribute . . . to the expansion of human knowledge of phenomena in the atmosphere and space. The Administration shall provide for the widest practicable and appropriate dissemination of information concerning its activities and the results thereof."

—NATIONAL AERONAUTICS AND SPACE ACT OF 1958

NASA SCIENTIFIC AND TECHNICAL PUBLICATIONS

TECHNICAL REPORTS: Scientific and technical information considered important, complete, and a lasting contribution to existing knowledge.

TECHNICAL NOTES: Information less broad in scope but nevertheless of importance as a contribution to existing knowledge.

TECHNICAL MEMORANDUMS: Information receiving limited distribution because of preliminary data, security classification, or other reasons.

CONTRACTOR REPORTS: Scientific and technical information generated under a NASA contract or grant and considered an important contribution to existing knowledge.

TECHNICAL TRANSLATIONS: Information published in a foreign language considered to merit NASA distribution in English.

SPECIAL PUBLICATIONS: Information derived from or of value to NASA activities. Publications include conference proceedings, monographs, data compilations, handbooks, sourcebooks, and special bibliographies.

TECHNOLOGY UTILIZATION PUBLICATIONS: Information on technology used by NASA that may be of particular interest in commercial and other non-aerospace applications. Publications include Tech Briefs, Technology Utilization Reports and Technology Surveys.

Details on the availability of these publications may be obtained from:

SCIENTIFIC AND TECHNICAL INFORMATION OFFICE

NATIONAL AERONAUTICS AND SPACE ADMINISTRATION

Washington, D.C. 20546